scientific reports

OPEN

Photocatalytic degradation of 3-monochloropropane-1,2-diol in aqueous solutions by selenium doped boron carbide nanoparticles

Mahin Velayati[1,2], Tahereh Rohani Bastami[3], Reza Kazemi Oskuee[1,4,5], Simin Nazarnezhad[6,7], Seyedeh Faezeh Taghizadeh[1], Hamid Ahmadpourmir[1], Hossein Ahmadzadeh[8]✉ & Ramin Rezaee[1]✉

3-monochloropropane-1,2-diol (3-MCPD) belongs to the chloropropanols family and it is a thermal processing contaminant that exerts renal and reproductive toxicities. This work aimed to synthesize boron carbide (B_4C) nanoparticles (NPs) and Se-doped B_4C-NPs (Se@B_4C-NPs) using the sol-gel approach. The photocatalytic activity of these NPs in removing 3-MCPD from aqueous solutions, was investigated based on changes in 3-MCPD levels as determined by UV-Vis spectrophotometry and liquid chromatography-tandem mass spectrometry (LC-MS/MS). Also, a pilot cytotoxicity evaluation was performed using MTT assay following treating human foreskin fibroblasts (HFFs) for 48 and 72 h with the two NPs. X-ray diffraction (XRD) and Field emission scanning electron microscopic (FE-SEM) analysis of the NPs confirmed that Se@B_4C-NPs had crystalline structures with spherical morphology. Also, treatment with Se@B_4C-NPs under optimum conditions (for 60 min at pH 7), effectively reduced 3-MCPD levels (by ~ 83%), which was greater than that observed for B_4C-NPs (by ~ 51%). Moreover, MTT results showed that these NPs at levels applied in the present work, did not produce significant toxicity. Based on our findings, Se@B_4C-NPs can be considered a promising tool for mitigating 3-MCPD levels in aqueous solutions.

Keywords 3-monochloropropane-1,2-diol (3-MCPD), Biocompatibility, Boron carbide nanoparticles (B_4C-NPs), Photocatalytic degradation

Isomers of chloropropanediols are found in various foods containing hydrolyzed protein, such as condiments and salty foods[1]. Alpha-chlorohydrin or 3-monochloropropane-1,2-diol (3-MCPD) is a contaminant resulting from the thermal processing of food and a by-product of processing or purifying edible oils and fats at high temperatures (> 200 ^{0}C, Table 1)[2]. At high temperatures, fatty compounds such as glycerols, acyl glycerols, and phospholipids react with hydrochloric acid to form 3-MCPD[3]. Members of the chloropropanol family have been identified in various foods[4–8]. Furthermore, low concentrations of chloropropanols were reported in drinking water from the UK[9].

Drinking water from water purification plants might be contaminated with 3-MCPD due to application of epichlorohydrin-linked cationic polymer resins[10,11]. In the paper industry, some types of epichlorohydrin-based wet-strength resins used in the paper and cellulose casings contain 3-MCPD. In this context, polyamide epichlorohydrin (PAE) is added to paper food packaging materials to improve their wet strength. PAE is

[1]Applied Biomedical Research Center, Basic Sciences Research Institute, Mashhad University of Medical Sciences, Mashhad, Iran. [2]Student Research Committee, Mashhad University of Medical Sciences, Mashhad, Iran. [3]Department of Chemical Engineering, Faculty of Advanced Technologies, Quchan University of Technology, Quchan 94771-77870, Iran. [4]Department of Medical Biotechnology and Nanotechnology, Faculty of Medicine, Mashhad University of Medical Sciences, Mashhad, Iran. [5]Targeted Drug Delivery Research Center, Mashhad University of Medical Sciences, Mashhad, Iran. [6]Tissue Engineering Research Group (TERG), Department of Anatomy and Cell Biology, School of Medicine, Mashhad University of Medical Sciences, Mashhad, Iran. [7]Metabolic Syndrome Research Center, Mashhad University of Medical Sciences, Mashhad, Iran. [8]Chemistry Department, Faculty of Science, Ferdowsi University of Mashhad, Mashhad 1436-91779, Iran. ✉email: h.ahmadzadeh@um.ac.ir; hossein.ahmadzadeh@gmail.com; rezaeera@mums.ac.ir; raminrezaee1983@gmail.com

IUPAC name and synonyms	Chemical formula	Structure
3-Chloropropane-1,2-diol α-Chlorohydrin, α-Glycerol chlorohydrin, α-Monochlorohydrin, 3-MCPD	$CH_3CH(OH)CH_2OH$	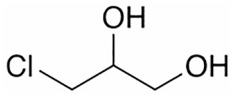

Table 1. Chemical structure of 3-MCPD.

often produced from epichlorohydrin and 3-MCPD is a by-product of epichlorohydrin; slow hydrolysis of epichlorohydrin has been observed in aqueous media[12].

Untoward health effects of 3-MCPD include neurotoxicity, nephrotoxicity, and reproductive toxicity[13,14] and it is regarded as a 2B-group carcinogen for humans by the International Agency for Research on Cancer (IARC)[10]. 3-MCPD is found in both free and esterified forms and the European Food Safety Authority (EFSA) considers a tolerable daily intake (TDI) of 2 µg/kg BW/day for 3-MCPD and its fatty acid esters.

Advanced oxidation processes (AOPs) have been extensively studied for removing organic pollutants from water sources[15,16]. AOPs include photochemical reactions such as photocatalysis, photo-Fenton reactions, electrochemical reactions such as electro-Fenton, and physical approaches such as ultrasound, which act based on producing active free radicals[17]. These free radicals have great oxidizing power and can destroy and mineralize organic pollutants. The photocatalytic approach to decompose harmful organic contaminants in water has received considerable attention because of its highly environmentally friendly and low-cost nature. In this method, semiconductors with a high photocatalytic activity that are activated by a light source, are used[18,19].

Nanoparticles (NPs) can be prepared using various chemical, physical, and biological methods[20,21]. Chemical and physical methods include, but are not limited to, hydrothermal[22] plasma[23] microemulsion[24] sol-gel[25] sonochemical[26]pulsed laser[27] solvothermal[28] and electrochemical methods. In recent years, researchers have taken advantage of green chemistry to synthesize NPs. The green synthesis method is eco-friendly, non-toxic, cost-effective, fast, and high-yielding, and most importantly, it uses biodegradable materials[29].

Boron carbide (B_4C) is a p-type, metal-free semiconductor used in the photocatalytic process[30]; it is one of the hardest materials due to the existence of characteristic B–C, and B–B bonds. B_4C has high electrical conductivity and chemical stability while exerting low toxicity, and it is costly to prepare[31]. Furthermore, B_4C has a low bandgap, exhibiting strong visible light absorption and high oxidation resistance[32]. Doping with metals, non-metal and metal oxides fundamentally improves a photocatalyst's physical and chemical properties and thus, its photocatalytic performance[33,34]. Non-metallic materials have favorable redox potential and good charge mobility, they are able to reduce electron-hole pair recombination, and they exert acceptable chemical stability, all improving photocatalytic reactions[35]. Selenium doping with NPs enhances the NPs' photocatalytic activity by modifying the electronic band structure or creating intermediate energy levels[36]. Despite considerable efforts made to reduce 3-MCPD levels in different matrices[37,38] based on the literature, there is no report on the potential photocatalytic activity of Se-doped B_4C-NPs (Se@B_4C-NPs) for the removal of 3-MCPD and other pollutants such as dyes from aqueous solutions.

To the best of our knowledge, in this study for the first time, Se@B_4C-NPs were synthesized by the sol-gel method at low temperature, and its efficiency for removal of 3-MCPD from aqueous solution under visible light, was investigated. To have an insight into potential cytotoxicity of the synthesized NPs, the viability of human foreskin fibroblasts (HFFs) was assessed following 48- and 72-hour treatment using MTT (3-[4,5-dimethylthiazol-2-yl]-2,5 diphenyl tetrazolium bromide) assay.

Materials and methods

Chemicals

3-monochloropropane-1,2-diol (3-MCPD), sodium selenite (Na_2SeO_3), polyvinyl alcohol (PVA), and boric acid (H_3BO_3, BA) were procured from Merck (Germany).

Synthesis of B_4C-NPs

B_4C-NPs were synthesized from polyvinyl borate (PVBO) precursor. The PVBO precursor was produced by the condensation reaction of PVA as a carbon source and BA (PVA (O-H group): BA molar ratio 4.2:1). For the synthesis of PVBO precursor, first, PVA (solution A: 2.74 g of PVA + 100 mL of distilled water (PVA is not soluble in cold water and it was dissolved in distilled water by stirring and heating in a water bath at 80 °C to facilitate the dissolution of PVA in water)) and BA (solution B: 0.86 g of BA + 30 mL distilled water) were prepared; then, solution B was added dropwise to solution A at 80 °C while stirring. In the continuation, PVBO precursor as a white gel was produced and heated until the water was completely evaporated. Next, the PVBO precursor was kept in an oven at 120 °C for 4 h. Then, the resulting white gel was powdered using an agate mortar and pyrolyzed to produce B_4C-NPs. At the end, the produced PVBO powder was placed in alumina crucibles, calcinated at 400 °C in the air for 2 h, and then, heat-treated at 1300 °C for 4 h in Ar flow (5 °C /min), yielding a black powder of B_4C-NPs[39].

Synthesis of Se@B_4C-NPs

Synthesis of Se@B_4C-NPs followed a process similar to that used for pure B_4C-NPs synthesis; however, Se@B_4C-NPs synthesis was carried out at a lower temperature. First, PVA was prepared as stated above. Then, 0.112 g sodium selenite was added to the PVA solution and the resulting suspension (Se-PVA suspension) was stirred for 1 h. Next, BA solution was prepared as shown above and added dropwisely to the Se-PVA suspension at

80 °C, yielding PVB/Se precursor as a white gel. Then, the white gel was dried at 120 °C for 4 h, powdered, and calcined at 800 °C for 2 h (in air, 5 °C/min). Finally, a black powder of Se@B_4C-NPs was achieved[40]. The protocol employed for the synthesis of the NPs is illustrated in Fig. 1.

Characterization of B_4C-NPs and Se@B_4C-NPs

Different techniques were used to characterize the synthesized Se@B_4C-NPs. X-ray diffraction (XRD) analysis was done by Rigaku D/max-250 to examine the crystalline nature of the synthesized materials. Structural and bonding properties of NPs were analyzed based on Fourier transform-infrared (FT-IR) spectra recorded by a Shimadzu IRPrestige-21 spectrometer. The surface morphology of NPs was assessed through Field emission scanning electron microscopic (FE-SEM) and the percentage of the elements was determined using the Energy-dispersive X-ray spectroscopy (EDX) examination, using Hitachi-SU8010. The Transmission Electron Microscopy (TEM, JEOL JEM-2000EX) was implemented for determining the shape and size of NPs. The zeta potential (ZP) and Dynamic Light Scattering (DLS) were examined by Particle Size Analyzer (Horiba, SZ-100). Inductively Coupled Plasma optical emission spectroscopy (ICP-OES) measures and identifies elements in NPs. Thermogravimetric analysis (TGA) of the PVBO precursor was carried out from room temperature up to 1100 °C at a heating rate of 10 °C/min in the air atmosphere, using NETZSCH STA449. The UV-visible diffuse reflectance spectroscopy (UV-Vis/DRS) spectra were obtained to analyze the optical attributes of NPs. Also, to ascertain the charge carrier separation, the samples' photoluminescence (PL) spectra were obtained using a fluorescence spectrophotometer (F-2700, Hitachi) at room temperature.

Assessment of photocatalytic activity of the NPs for removal of 3-MCPD from aqueous solution

Photolysis

In the present work, a control group that underwent photolysis only (i.e. was not treated with the NPs) was considered to assess the effect of the catalysts. In these experiments, degradation of 3-MCPD (100 µg/mL, pH 7) after 60 min of LED light irradiation (SMD LED, 50 W) at room temperature, was examined using UV-Vis spectroscopy.

Photocatalytic process

The photocatalytic activity of the synthesized B_4C-NPs and Se@B_4C-NPs was investigated at the optimized conditions (catalyst dose 50 mg, pH 7, and LED light irradiation intensity 50 W). To achieve this goal, 50 mg of the catalyst was dispersed into 50 mL aqueous solution of 3-MCPD (making a 100 µg/mL stock solution, reaching pH 7). Then, the mixture solution was stirred in the dark at room temperature for 45 min to achieve adsorption and desorption equilibrium. Then, it was exposed to visible irradiation light (i.e. SMD LED) with continuous stirring for 60 min. During this interval, every 15 min, 2 mL of the NPs-treated 3-MCPD solution was centrifuged at 12,000 rpm for 10 min and the absorbance of the clear solution was measured by UV-Vis spectroscopy[41]. In the pH study, the initial pH was adjusted with NaOH solutions. Furthermore, 3-MCPD level

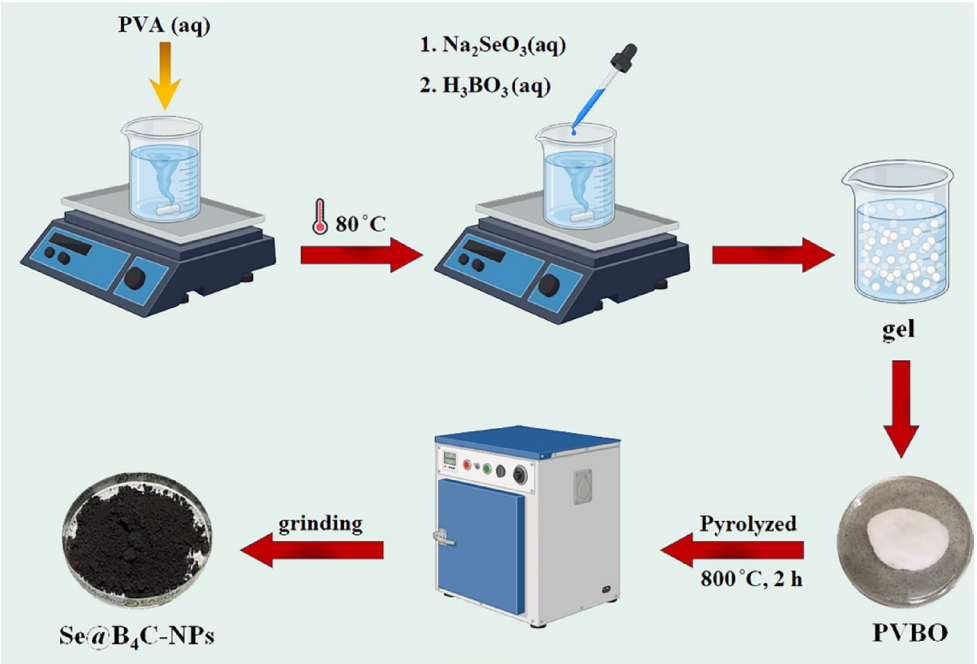

Fig. 1. Schematic synthesis of Se-doped boron carbide nanoparticles (Se@B_4C-NPs). *PVA* Polyvinyl alcohol, *PVBO* Polyvinyl borate, *aq* Aqueous solution. This Figure was created with BioRender.com.

before and after treatment with NPs (at the 60th min) was measured by Liquid chromatography-tandem mass spectrometry (LC-MS/MS) analysis (as described in 2.6.).

Assessment of the roles of reactive species and holes in photocatalysis
The role of the reactive species superoxide ($^{\circ}O_2^-$), hydroxyl (OH°), and holes (h^+) in the observed removal of 3-MCPD, was assessed using selective scavengers 1,4-benzoquinone (BQ), isopropyl alcohol (IPA), and sodium hydrogen carbonate (NaH), respectively, under optimal conditions[42].

LC-MS/MS analysis of 3-MCPD

LC-MS/MS condition
The liquid chromatography (LC) was performed using a Shimadzu (Shimadzu, Japan) system equipped with a Kromasil 100-5 C18 column (150 mm × 4.6 mm, 3 µm). The temperature of the column was set at 30 °C. Mobile phase included 95% CH_3OH and 0.1% formic acid (phase A), and 5% water with 0.1% formic acid (phase B). The flow rate and injection volume were 0.25 mL/min and 7 µL, respectively.

The LC-MS/MS analysis was performed in negative ionization mode (ESI–) using Q1M1 scan mode on an AB Sciex 3200 QTRAP instrument. The gas pressure (N_2, purity > 99.98%) was 30 psi. The quantifier ion was m/z 155.3, corresponding to the formate adduct $[M+HCOO]^-$ of 3-MCPD. This ion provided the highest sensitivity and selectivity for quantification. Results were analyzed using AB Sciex Analyst software (version 1.6.3).

LC-MS/MS analysis specifications
The linear dynamic range (LDR) of the analysis was determined using four concentrations of 3-MCPD (6.25, 12.5, 25, and 50 µg/mL) prepared in distilled water and injected into the LC-MS/MS apparatus. A linear standard curve (Fig. 2) was obtained within the concentration range of 6.25–50 µg/mL for 3-MCPD. From the regression analysis, the following linear equation was obtained: $y = 375.66x + 12{,}572$, with R^2 equal to 0.9745, indicating a linear relationship between 3-MCPD concentration and the area under the peak[2].

Assessment of NPs cytotoxicity using MTT assay

The MTT assay is the most well-known test used for cell viability evaluation. This colorimetric assay is based on the activity of mitochondria, breakdown of yellow tetrazolium crystals by the enzyme succinate dehydrogenase and formation of insoluble purple crystals[43]. Only living cells with active mitochondria can convert the MTT solution into the water-insoluble purple formazan precipitate[44]. To evaluate the potential cytotoxic properties of the prepared B_4C-NPs and Se@B_4C-NPs, this assay was performed on human foreskin fibroblasts (HFFs). This cell.

line was purchased from the Pasteur Institute (Tehran, Iran). The cells were cultured in Dulbecco's Modified Eagle Medium (DMEM) supplemented with 10% (v/v) fetal bovine serum (FBS) and 1% v/v antibiotic (penicillin/streptomycin) (PAN-Biotech, Minneapolis, MN, USA) and incubated in a humidified atmosphere (37 °C and 5% CO_2). Briefly, 5×10^3 cells per well were seeded in a 96-well microliter plate. HFFs were treated with NPs at a concentration range of 15.6–1000 µg/mL for 48 and 72 h. Afterwards, 10 µL of MTT solution was added to each well to reach a final concentration of 0.5 mg/mL and incubated for 3–4 h. Then, the culture media were gently removed and replaced with 100 µL of dimethyl sulfoxide (DMSO, Sigma-Aldrich) to dissolve the purple formazan crystals, and the plates were incubated in the dark for 20 min. Finally, cell viability was calculated by measuring the absorbance of each well at 570 nm and 690 nm using a microplate reader (Epoch, BioTek, Westmont, IL, USA)[41]. Data was analyzed using one-way analysis of variance (ANOVA) by GraphPad Prism Software (Ver. 10.3.0).

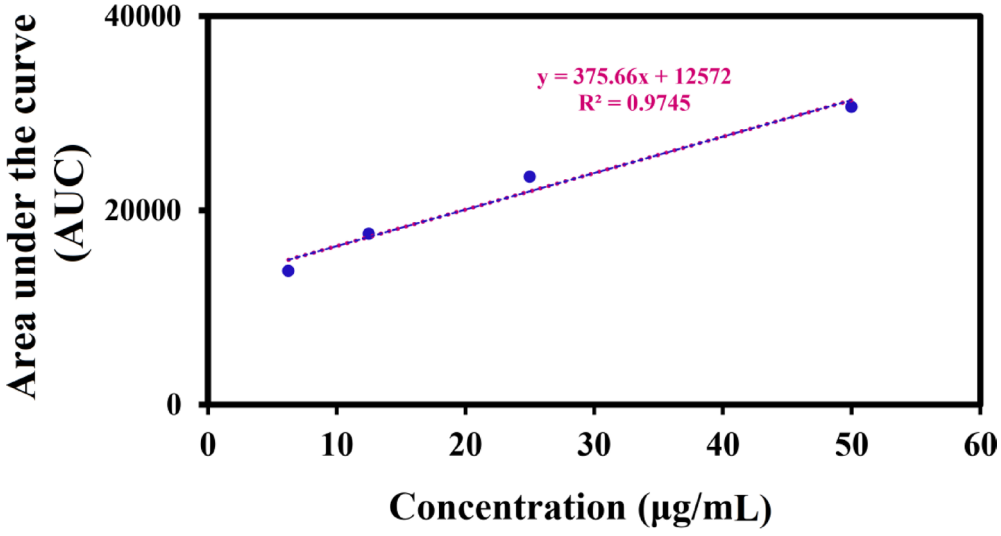

Fig. 2. Standard curve plotted for 3-MCPD prepared in distilled water.

Results

FT-IR analysis

FT-IR analysis was performed to confirm the formation of PVBO precursor, B_4C-NPs, and Se@B_4C-NPs. According to the FT-IR spectrum of PVBO (Fig. 3a), the main absorption bands were observed at 1123, 1285, 1335, 1425,1735, 2940, and 3437 cm^{-1}, which is in line with a previous study's findings on B_4C[39]. The transmittance at 3437 cm^{-1} corresponds to the stretching vibrations of O-H, which were lower than that recorded for PVA (Fig. 3a). This result suggests the conversion of the OH group in esterification and the existence of unreacted OH groups. The transmittance at 1285 and 1123 cm^{-1} was attributed to stretching bonds of B-O-C, confirming the occurrence of PVA chain cross-linking with BA. The transmittance at 1285, 1335, 1425, 1735, and 2940 cm^{-1} was ascribed to the bending band of C-H, stretching bands of B-O, C = O, C-H, and O-H, respectively. In addition, the absorption band at 1198 cm^{-1} (Fig. 3a (BA spectrum)) confirmed the deformation of the B-OH band, which disappeared in PVBO spectrum. A schematic presentation of the esterification reaction suggested by Fathi et al. is given below[45].

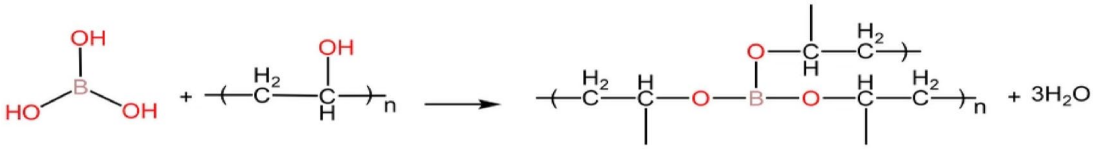

In the FT-IR spectrum obtained for B_4C-NPs (Fig. 3b), the peaks remarked at 420–520 cm^{-1} were attributed to the C-B-C bonds, and the peaks at 690, 838, 1231, and 1570 cm^{-1} were assigned to the stretching band of B-C, and the peak at 1683 cm^{-1} was attributed to the asymmetrical stretching of B-C. The transmittance peaks for B-C and C-B-C bonds indicated the complete reaction between BA and PVA, proving the formation of the B_4C structures. These values agree with those reported by Aydın and Tuncer for B_4C[46]. Se@B_4C-NPs spectrum (Fig. 3c) indicates that the stretching bonds of B-C were shorted and shifted by the interaction of B and C with Se. The peaks belonging to the B_4C bond demonstrated that Se-doped PVBO was converted to Se@B_4C-NPs at a relatively low heat treatment temperature[47].

Thermal gravimetric analysis (TGA)

The TGA analysis focuses on the relationship between the weight changes and the temperature[48]. Figure 4 displays the TGA thermogram of PVBO. TGA findings were similar for PVBO and PVBO/Se. It was observed that the dehydration of PVBO commenced at 310 °C. This temperature is higher compared to the decomposition temperatures of PVA (250 °C) and BA (110 °C), implying that the formation of B–O–C bonds in the PVBO significantly enhances its thermostability[49]. Additionally, the weight losses above 400 °C were attributed to removing the polymer side groups, followed by the breakdown of the precursor backbone. Based on these findings, PVBO precursor underwent pyrolysis at temperatures above 400 °C. Therefore, a heat treatment at 400 °C in air for 2 h was applied to the precursor, followed by pyrolysis at 1300 °C in Ar flow for 4 h for B_4C-NPs synthesis[50] and at 800 °C in air for 2 h for Se@B_4C-NPs synthesis.

X-ray diffraction (XRD) spectra

The crystalline nature of the synthesized NPs was analyzed using XRD patterns. XRD patterns of B_4C-NPs (at both 400 °C and 1300 °C) and Se@B_4C-NPs (800 °C) (Fig. 5) showed successful synthesis of B_4C-NPs and Se@B_4C-NPs. The NPs prepared at 400 °C showed an amorphous structure but B_4C-NPs were not formed; however, at 1300 °C in Ar flow, B_4C-NPs were synthesized with a crystalline structure and thus, this condition was chosen. As Fig. 5 shows, no peak was observed for B_4C-NPs. The XRD pattern exhibits pronounced peaks confirming the crystalline nature of B_4C-NPs (1300 °C) and Se@B_4C-NPs. The diffraction peaks (B_4C-NPs 1300 °C spectra) at 2θ of 19.67°, 22.04°, 23.47°, 31.02°, 34.97°, and 37.82° matched with (101), (003), (012), (110), (104), and (021) crystalline planes, respectively. These particular peaks were indexed to a rhombohedral phase of B_4C-NPs (JCPD # 35–0798). Also, a broad diffraction peak was observed at 2θ around 25° which was assigned to the amorphous carbon phase[51]. The Se@B_4C-NPs (800 °C) spectra, in addition to B_4C-NPs peaks, depict peaks of Se at 2θ of 23.63°, 29.42°, 41.67°, 43.46°, 44.82°, and 49.63° which matched with (100), (101), (110), (102), (111), and (201) crystalline planes, respectively (JCPD # 05-0362). Furthermore, the average crystallite size of B_4C-NPs and Se@B_4C-NPs was about 30 and 22 nm, respectively, as calculated using Scherer's equation (Eq. 1)[52].

$$D = k\,\lambda / \beta \cos\theta \tag{1}$$

D: crystalline size (nm)
λ: 0.154 nm
β: FWHM = Full Width at Half Maximum
θ: Bragg angle (degree)

FE-SEM/ particle size analysis (PSA)/ EDX/ inductively coupled plasma optical emission spectroscopy (ICP-OES) analysis

The surface morphology and size distribution of the NPs were examined using FE-SEM /PSA/EDX analysis. The resulting images are displayed in Fig. 6 a,b,c,d,e,f). The FE-SEM/PSA carried out for B_4C-NPs and Se@

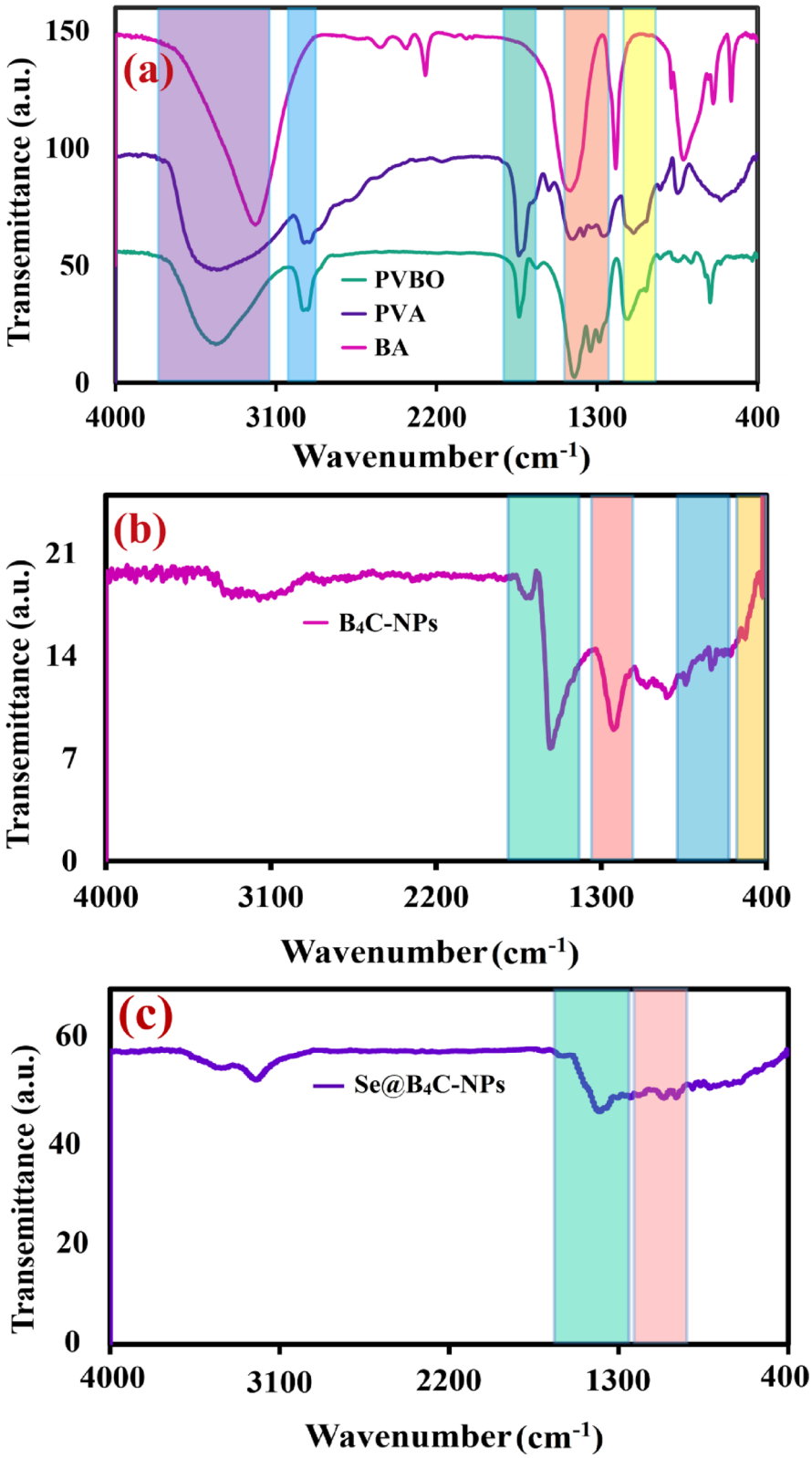

Fig. 3. FT-IR spectrum of (**a**): BA (pink spectrum), PVA (purple spectrum), and PVBO (green spectrum), (**b**) B_4C-NPs, and (**c**) Se@B_4C-NPs. *PVA* Polyvinyl alcohol, *PVBO* Polyvinyl borate, and *BA* boric acid (H_3BO_3).

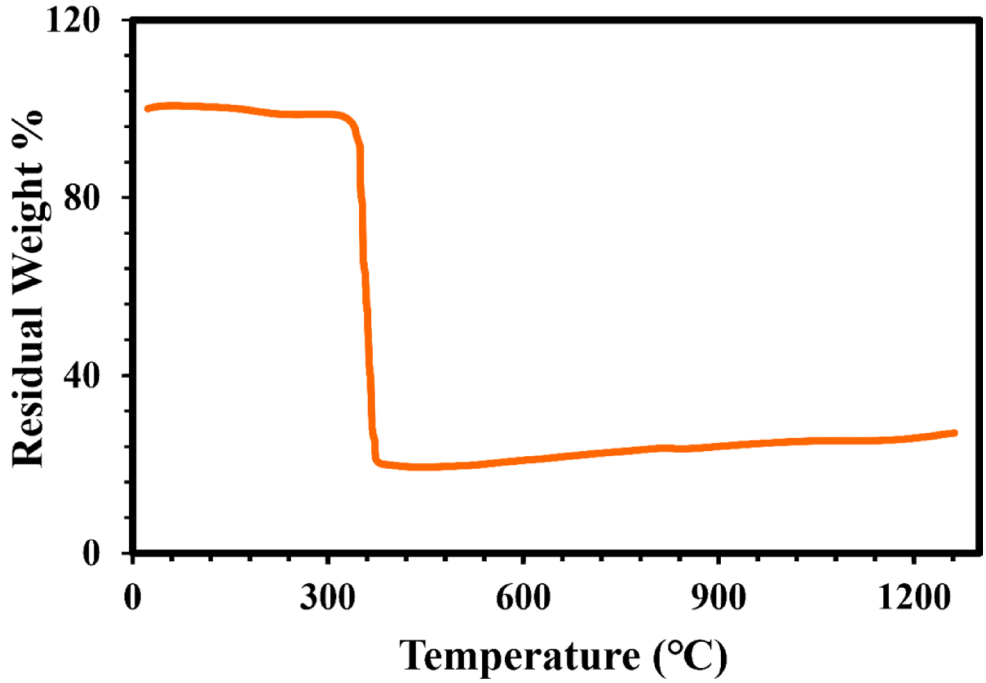

Fig. 4. Thermal gravimetric analysis (TGA) curve of PVBO precursor.

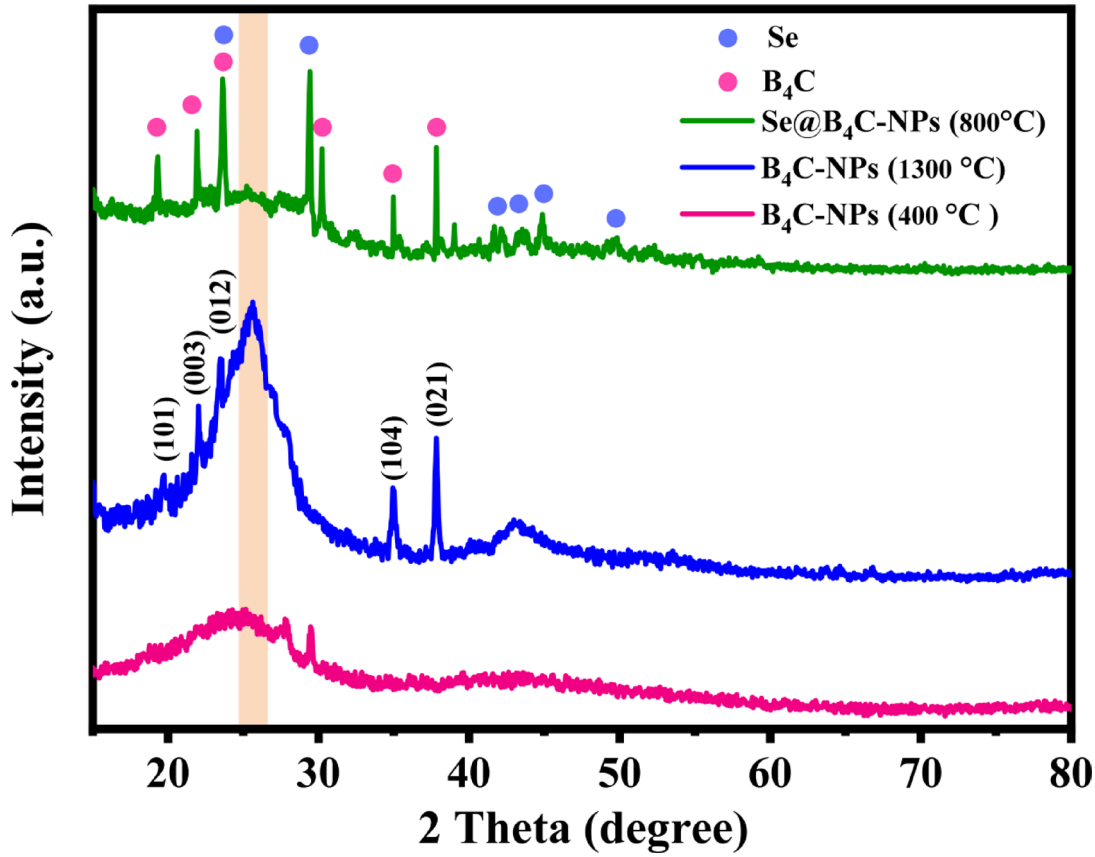

Fig. 5. X-ray diffraction (XRD) pattern of B_4C-NPs (400 °C in air flow (pink spectrum)), B_4C-NPs (1300 °C in Ar flow (blue spectrum)), and Se@B_4C-NPs (800 °C in air flow (green spectrum)).

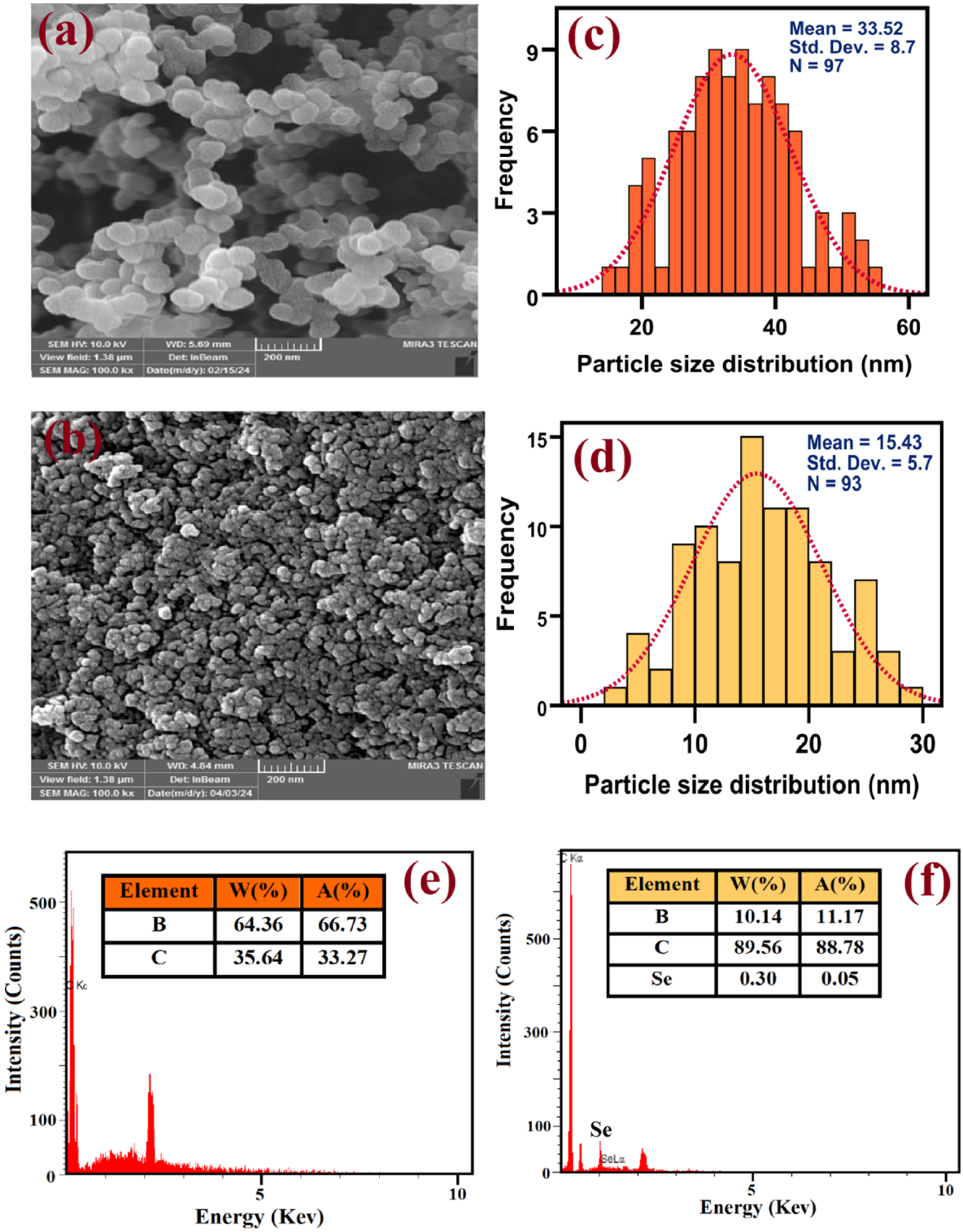

Fig. 6. FE-SEM/PSA/EDX examination of B_4C-NPs (**a**, **c**, and **e**) and Se@B_4C-NPs (**b**, **d**, and **f**). *FE-SEM* Fieldemission scanning electron microscope, *PSA* Particle size, *EDX* Energy-dispersive X-ray spectroscopy. (*W(%)* Weight%, and *A(%)* Atomic percent).

B_4C-NPs showed spherical morphology with an average size of 33 and 15 nm, respectively (Fig. 6a,b,c,d). Also, EDX analysis indicated the presence of elements C and B in B_4C-NPs, and C, B, and Se in Se@B_4C-NPs structure as shown in Fig. 6e,f which was in line with a previous report[53]. Figure 7a–e shows the mapping analysis of Se@B_4C-NPs where the presence of Se in NPs was confirmed. Further, Se level analyzed by ICP-OES in doped samples, is reported in Table 2.

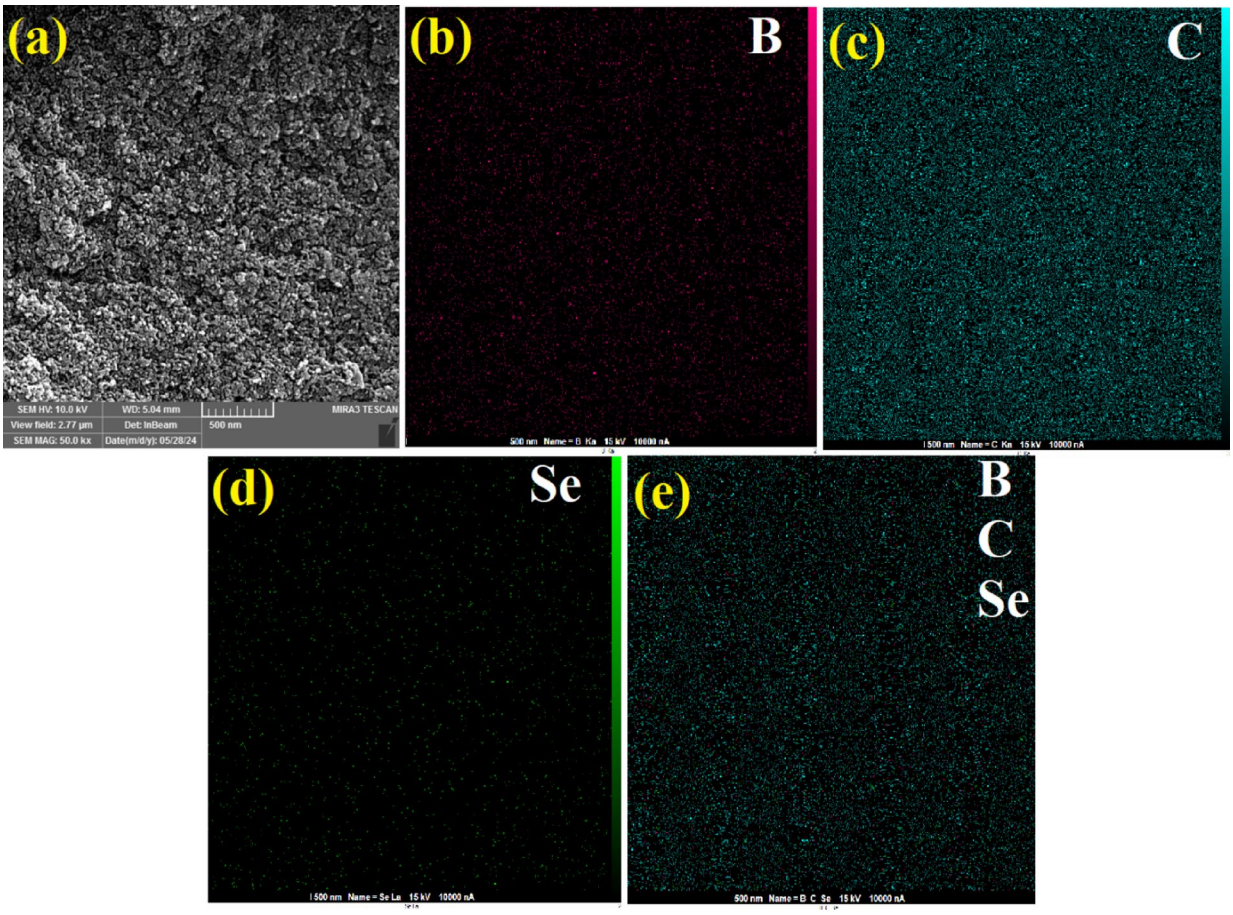

Fig. 7. Mapping analysis of Se@B_4C-NPs (**a**) original FE-SEM image; (**b**) boron element, (**c**) carbon element, (**d**) selenium element, and (**e**) all elements.

Sample	Se amount (mean ± SD%)	LOD (μg/mL)*
Se@B_4C-NPs (5%)	0.3 ± 0.01	0.0094

Table 2. ICP-OES analysis of se level in se@B_4C-NPs. **LOD* Limit of detection.

Dynamic light scattering (DLS)/ zeta potential (ZP) measurement

The stability and size of B_4C-NPs, and Se@B_4C-NPs, were respectively measured by ZP and DLS analysis (Fig. 8a,b,c,d). The ZP measures the charge on the surface of NPs[47]. In the present study, the ZP of B_4C-NPs, and Se@B_4C-NPs was − 40 mV and − 51.60 mV, respectively (Fig. 8c,d). Also, according to the DLS analysis, the B_4C-NPs, and Se@B_4C-NPs showed a size of 111 ± 5.55 nm and 134 ± 6.04 nm, respectively, and with a polydispersity index (PDI) of about 0.21 and 0.32, respectively.

Transmission electron microscopy (TEM) images

The morphology and particle size distribution of Se@B_4C-NPs are shown in Fig. 9a,b. TEM image highlights the monotonous spherical morphology with a proximate diameter of 10.40 nm for Se@B_4C-NPs.

UV-visible diffuse reflectance spectroscopy (UV-Vis/DRS) and photoluminescence (PL) spectra

The optical properties of the synthesized NPs were investigated using UV-Vis/DRS. The UV-Vis/DRS findings are shown in Fig. 10. All synthesized samples had an absorption edge at about 700 nm (Fig. 10a), and this feature can enhance the photocatalytic properties of the NPs under visible light. The bandgap energy of the NPs was calculated through Eq. 2[54].

$$(F(R)h\nu)^n = A(h\nu - E_g) \quad (2)$$

A: Constant
R: Reflection coefficient

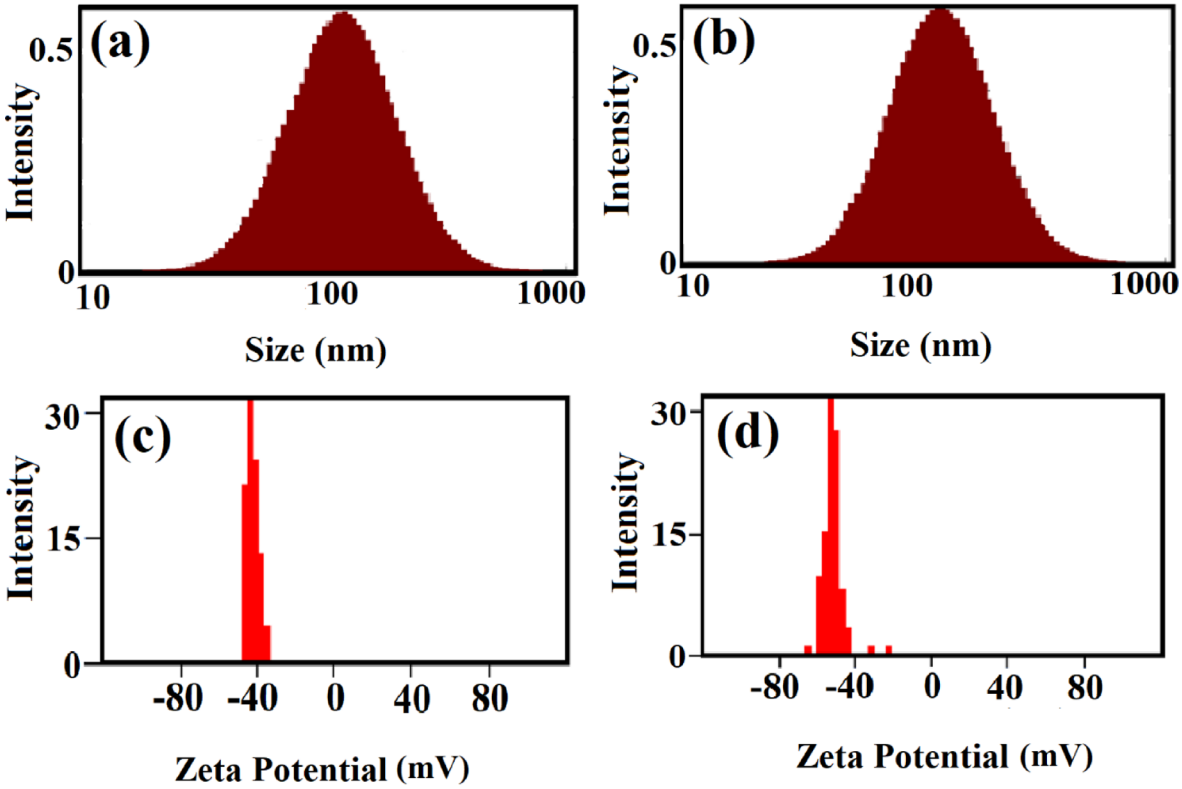

Fig. 8. The DLS (dynamic light scattering) and Zeta potential analysis of B_4C-NPs (**a** and **c**, respectively), and Se@B_4C-NPs (**b** and **d**, respectively).

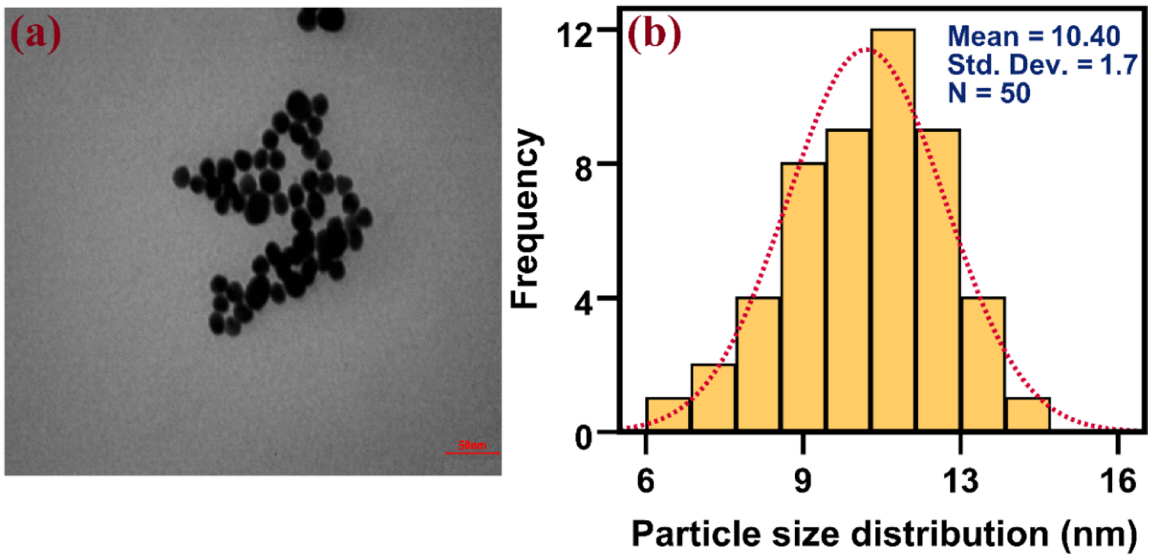

Fig. 9. TEM images (**a**) and PSA (**b**) of Se@B_4C-NPs.

hυ: Photon energy

The variation of $(F(R)h\nu)^n$ vs. hυ is exhibited in Fig. 10b. The bandgap energy values for B_4C-NPs and Se@B_4C-NPs were 1.57 eV and 1.46 eV, respectively. Interestingly, the bandgap of the synthesized nanomaterials was similar, confirming that B_4C-NPs and Se@B_4C-NPs had formed heterojunctions. The recombination rate of photogenerated electrons and holes plays an essential role in photocatalytic yield. The major issue with NPs is that the photo-generated electrons and holes possibly recombine, however, this can be overcome by the formation of heterojunctions between NPs and metals. Hence, to assess the formation of heterojunctions, PL spectra were recorded[55]. Figure 10c displays the PL spectra of B_4C-NPs and Se@B_4C-NPs. Compared with B_4C-

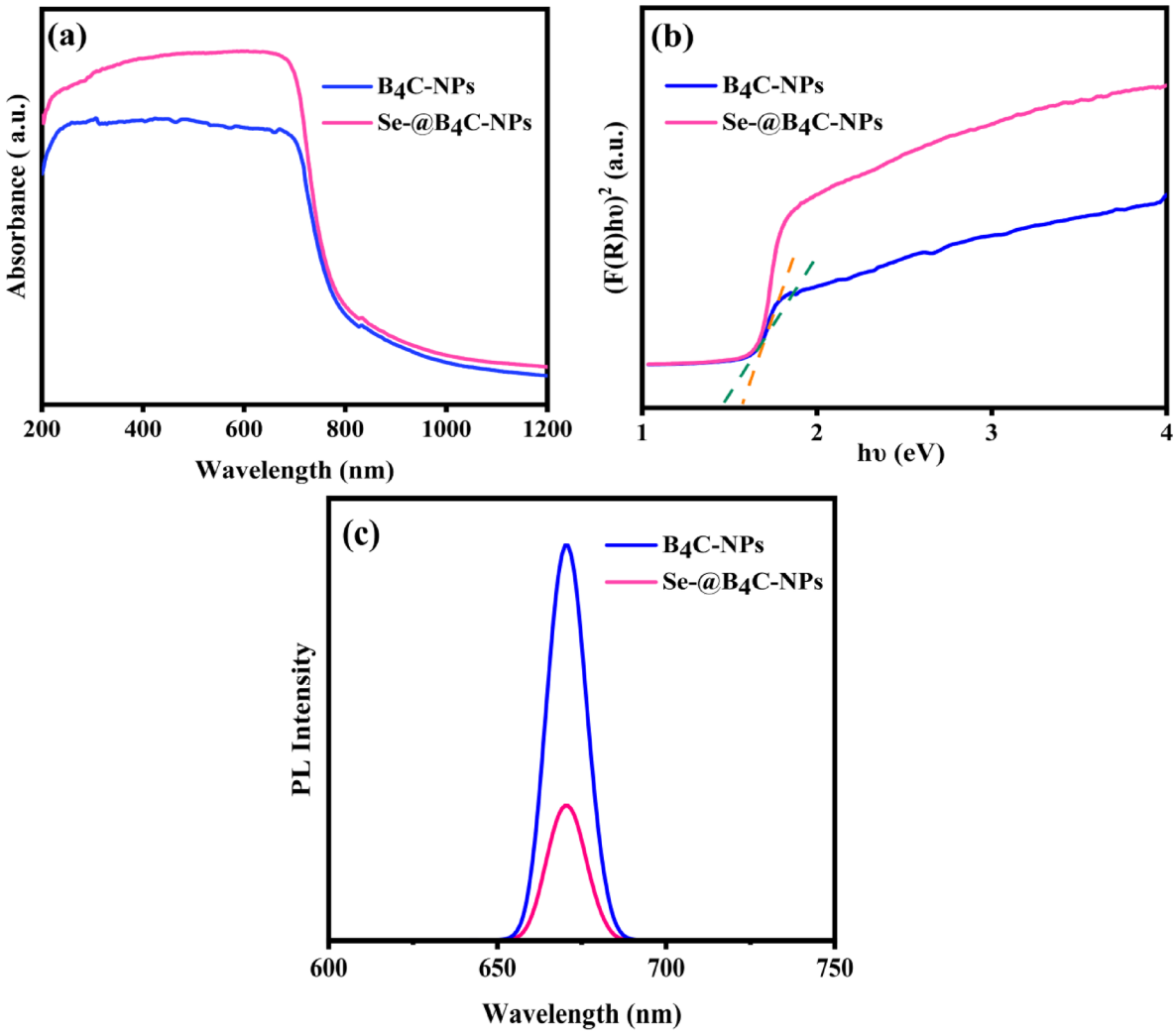

Fig. 10. UV-visible diffuse reflectance spectroscopy (UV-Vis/DRS) (**a**), bandgap energy (**b**), and Photoluminescence (PL) spectra (**c**) of B_4C-NPs, and Se@B_4C-NPs.

NPs, Se@B_4C-NPs showed a lower emission intensity which reflects significantly lower recombination of the electron-hole pairs[56].

Photocatalytic activity of B_4C-NPs and Se@B_4C-NPs for removal of 3-MCPD from aqueous solution

In Fig. 11a, UV–Vis spectrophotometric analysis of 3-MCPD following exposure to visible light (in the absence of the NPs), is presented. The 3-MCPD solution has an absorption peak of 278 nm. Results showed no obvious decrease in 3-MCPD concentration, indicating that the degradation of 3-MCPD did not happen under visible light only. Next, the synthesized B_4C-NPs and Se@B_4C-NPs were used as photocatalysts. The removal rate of 3-MCPD was calculated by Eq. 3[41], and the results are shown in Fig. 11b,c.

$$Degradation\,(\%) = \frac{A_0 - A_t}{A_0} \times 100 \tag{3}$$

A_0 and A_t: 3-MCPD concentration at 0 and 60 min, respectively.

The photodegradation rate of 3-MCPD for B_4C-NPs and Se@B_4C-NPs was 51% and 83% respectively as determined using UV-Vis spectrophotometry. Also, the analyte's level was determined using LC-MS/MS and results showed that treatment with B_4C-NPs and Se@B_4C-NPs under light exposure caused 56% and 88% reduction in 3-MCPD concentration. Both methods confirmed the reduction (at comparable rates) in the concentration of 3-MCPD. Therefore, our experiments confirmed that Se doping in B_4C increased its photocatalytic efficiency.

Figure 11c displays the 3-MCPD-absorbing performance of Se@B_4C-NPs in the dark (66% as determined by UV-Vis spectra and 73% as determined by LC-MS/MS analysis). This is probably due to the unique structure of Se@B_4C-NPs that provides a large surface area.

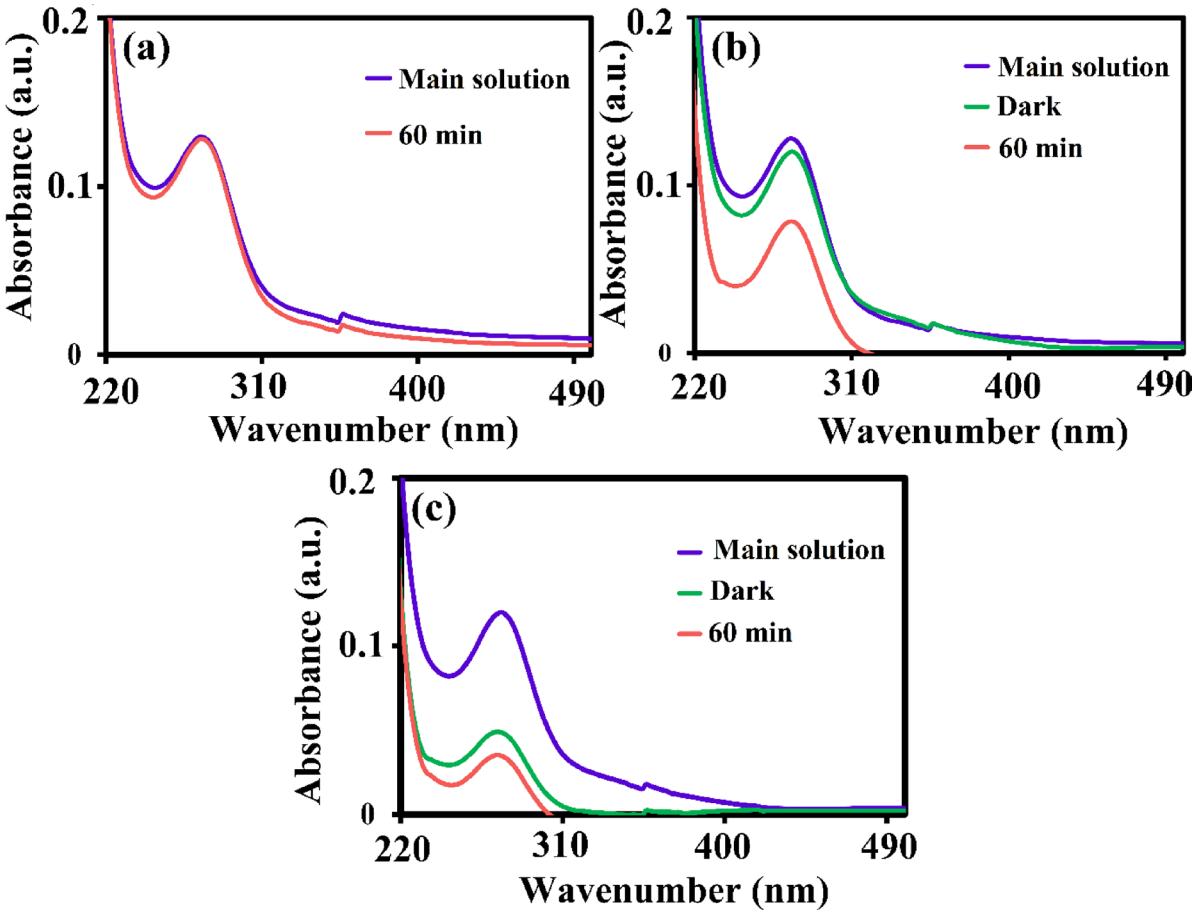

Fig. 11. The diagram of photolysis of 3-MCPD under visible light (**a**), the diagram of degradation of 3-MCPD by B_4C-NPs (**b**), and Se@B_4C-NPs (**c**) under optimal conditions ("Main solution" is the prepared 100-µg/mL stock solution of 3-MCPD), "Dark" represents absorbance following treatment with the NPs in the dark and "60 min" shows absorbance following treatment with the NPs under visible light).

Influence of NPs concentration

Photocatalytic activity is directly related to a catalyst dosage as with increasing levels of a catalyst higher degradation is expected[57]. This occurs as higher levels of a catalyst provide greater levels of free radicals required for the degradation process. However, once the optimum limit is reached, increasing the amount of catalyst does not speed up the process; this takes place as light penetration becomes difficult and renders most of the catalyst surface inactive[58,59]. In this study, we observed that increasing the concentration of Se@B_4C-NPs led to a higher photocatalytic degradation potential. As seen in Fig. 12a, the maximum degradation of 3-MCPD (i.e. 83%), was achieved with of 50 mg of Se@B_4C-NPs in 60 min.

Influence of pH

In this study, the degradation efficiency of 3-MCPD (100 µg/mL) using Se@B_4C-NPs (50 mg) increased with increasing pH, reaching its maximum at pH 7 and decreasing afterward (Fig. 12b). The initial pH of the 3-MCPD solution was 2.3; at this pH, no degradation was observed. When pH reached 7, an improvement in degradation was observed, which could be due to the interaction between OH^- ions and 3-MCPD molecules in a basic medium, resulting in the creation of a charge difference between Se@B_4C-NPs and 3-MCPD molecules, consequently, the Columbic attraction increases the interaction between the photocatalyst and 3-MCPD. For the pH value of 9, a possible explanation is that OH^- ions can interact with holes and become deactivated in basic conditions.

Influence of irradiation source

The light source is an essential part of photocatalytic degradation[60]. First, UV-Vis/DRS analysis was performed, and based on the obtained data, the bandgap energy was calculated using the Tauc equation. The bandgap energy values for B_4C-NPs and Se@B_4C-NPs were respectively 1.57 eV and 1.46 eV, implying that these NPs are active in the visible region, so, an LED light was chosen as the light source. However, to confirm the proper choice of LED as the light source, the photocatalytic process was also performed under UVA light (11 W). Figure 12c shows that the maximum degradation percentage was 25% under UVA light and 83% under visible light. This result was consistent with findings of UV-Vis/DRS and bandgap energy. Besides, the photocatalytic process was

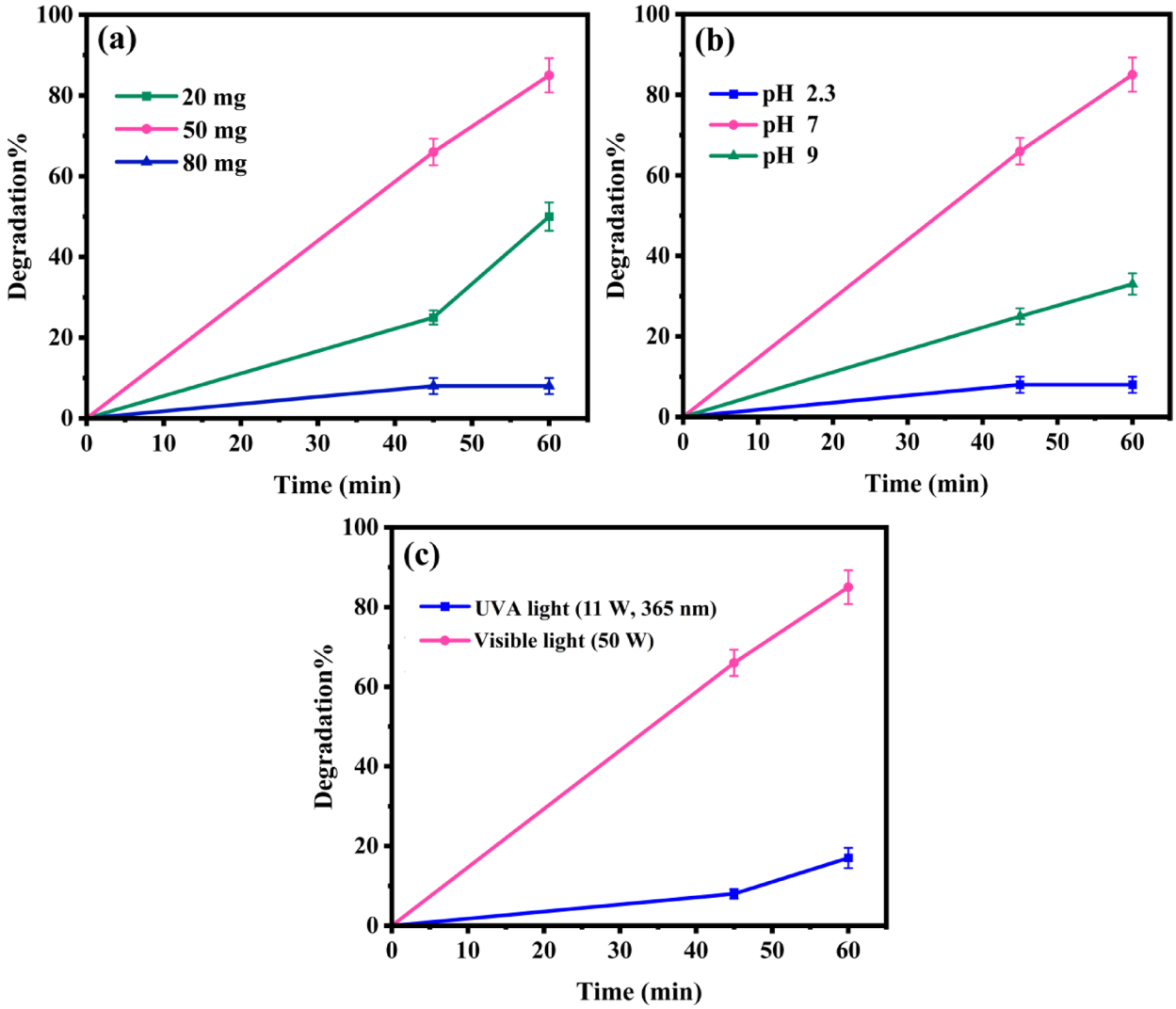

Fig. 12. The impact of catalyst dosage (**a**), initial pH (**b**), and light source (**c**) on degradation percentage.

performed for 120 min, and results showed that after 60 min, no degradation occurred. Therefore, the optimal time was determined to be 60 min.

Roles of reactive species and holes in photocatalysis

We observed that the photocatalytic activity of Se@B_4C-NPs was reduced in the presence of scavengers BQ and IPA, with IPA inducing the greatest effect. However, in the presence of NaH, the photocatalytic function was not affected (Fig. 13). The IPA and BQ induced a decrease in 3-MCPD degradation efficiency, indicating the contribution of reactive species OH° and $^{\circ}O_2^-$ to the degradation of 3-MCPD, with OH° potentially having a greater effect.

NPs cytotoxicity against HFFs

The effects of different concentrations of B_4C-NPs and Se@B_4C-NPs on HFFs viability are shown in Fig. 14. For both NPs, cell viability decreased with increasing doses following both 48 and 72 h exposure. B_4C-NPs had IC50 values of 741.1 µg/mL and 681.7 µg/mL after 48 and 72 h treatments, respectively. At both treatment periods, Se@B_4C-NPs at concentrations ≥ 250 µg/mL significantly reduced cell viability compared to the control group.

Discussion

The presence of 3-MCPD in a variety of food products and water resources is of concern due to its adverse health effects. Therefore, in the present study, we aimed at removing 3-MCPD from aqueous solution based on potential photocatalytic activity of B_4C-NPs and Se@B_4C-NPs. In a previous study, utilizing inorganic adsorbent materials (a synthetic magnesium silicate and a calcinated zeolite), 40% of palm oil 3-MCPDE was mitigated[37]. Another report indicated the efficiency of Metal-Organic Frameworks (MOF) and natural clays for 3-MCPD removal from edible oils[38].

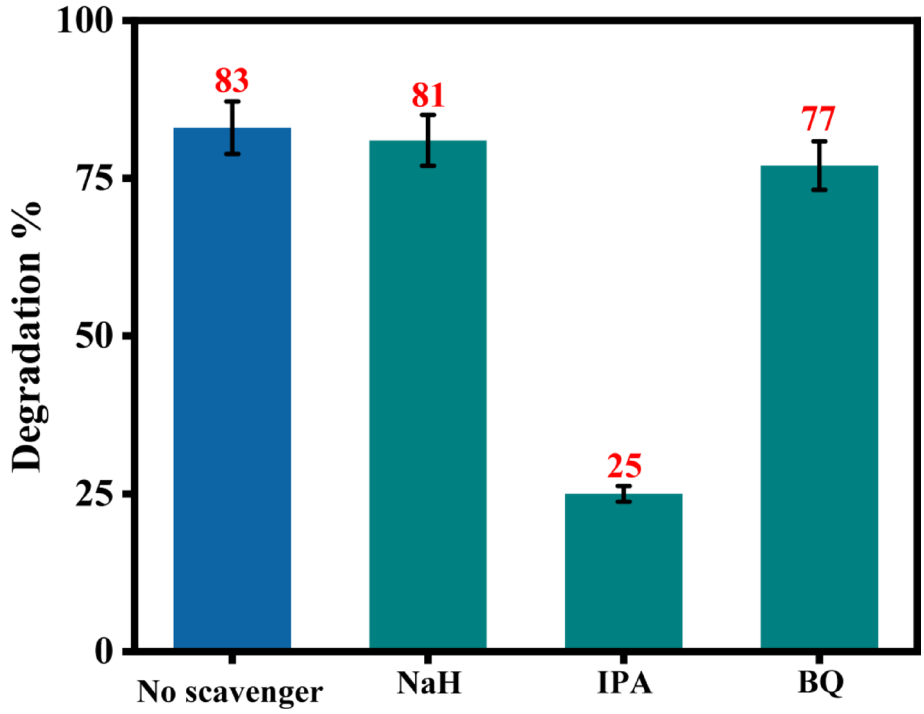

Fig. 13. Percentage of 3-MCPD degradation induced by Se@B_4C-NPs in the presence of 1,4-benzoquinone (BQ), isopropyl alcohol (IPA), and sodium hydrogen carbonate (NaH), in comparison to a no-scavenger group.

In our study, for the first time, we synthesized Se@B_4C-NPs at lower temperatures than pure B_4C-NPs and assessed its potential to remove 3-MCPD from aqueous solution by the photocatalytic process. According to the literature on the synthesis of B_4C-NPs[39,49] in this work, pyrolysis of polyvinyl borate (PVBO) precursor at 400, 500, 650, 700, and 800 °C in air for 2 h and then heat-treatment at 1300 °C for 4 h in Ar flow, was considered. The XRD patterns displayed that pyrolysis at 400 °C in air and heat-treatment at 1300 °C in Ar flow produced a crystalline structure, while under other conditions, the synthesized NPs were amorphous. In addition, TGA analysis showed that the initial calcination temperature was 400 °C. When B_4C-NPs were doped with Se, a crystalline structure was obtained under pyrolysis with air at 800 °C, in the absence of Ar flow. FT-IR confirmed the successful formation of PVBO from PVA and BA. The XRD patterns showed that the crystalline structure of B_4C-NPs was retained in Se@B_4C-NPs after Se incorporation. In addition, in the XRD pattern of Se@B_4C-NPs, there was no evidence of B_2O_3 peak at $2\theta = 25°$, indicating that Se can act as a catalyst and reduce the reaction temperature and time because compared to pure B_4C-NPs, Se@B_4C-NPs were synthesized with a high crystalline structure at 800 °C within 2 h. The calculated crystallite sizes of 30 nm and 22 nm respectively for B_4C-NPs and Se@B_4C-NPs, further confirmed the successful synthesis of the NPs. Therefore, this analysis confirmed that temperature plays an important role in determining the structural integrity, stability, and functional properties of NPs. The temperature of NPs synthesis process affects the nucleation rate and growth kinetics and can influence the shape and size of NPs. Higher temperatures may lead to increased kinetic energy, resulting in faster growth rates and potentially larger particle sizes. They can also affect the crystallinity and stability of NPs and the catalytic activity of NPs can be temperature-dependent[61]. Higher temperatures may enhance reaction rates but can also lead to deactivation or sintering of the catalyst[62]. FE-SEM/TEM images showed the successful anchoring of Se onto B_4C-NPs without causing significant changes in their morphology. Also, Se@B_4C-NPs had a narrower particle size distribution and smaller mean particle size than B_4C-NPs which is consistent with a previous report on doping Se with NiO-NPs[63]. The doping-induced reduction of particle size increases the surface area, thus enhancing photocatalytic activity[64]; the present work showed similar results in terms of photocatalytic activity. DLS analysis indicated stable dispersions which are crucial for practical applications. According to the DLS analysis, B_4C-NPs, and Se@B_4C-NPs showed a size of 111 ± 5.55 nm and 134 ± 6.04 nm, respectively. With a uniform distribution, EDX analysis confirmed the presence of C, B, and Se in NPs. Se@B_4C-NPs with a narrow bandgap energy of about 1.46 eV showed their suitability in absorbing light in the visible range. The difference in particle size measured by XRD and DLS is due to the difference in the measurement principles of the two methods[65]. DLS is a physical, non-destructive, and rapid method used to determine the size distribution of particles in solution. It is a measurement of the hydrodynamic diameter of particles in suspension. The size obtained by this method can be larger than that obtained by other techniques such as FE-SEM because the hydrodynamic diameter (size) in colloidal solutions includes the particle core, the adsorbed solvent layer, and any particle aggregation[66] while the XRD analysis determines the phase of crystals and the size of crystals[67]; therefore, the size obtained by DLS is expected to be larger than the size obtained by XRD. It should also be noted that particle aggregation in the suspension used in DLS can lead to greater particle

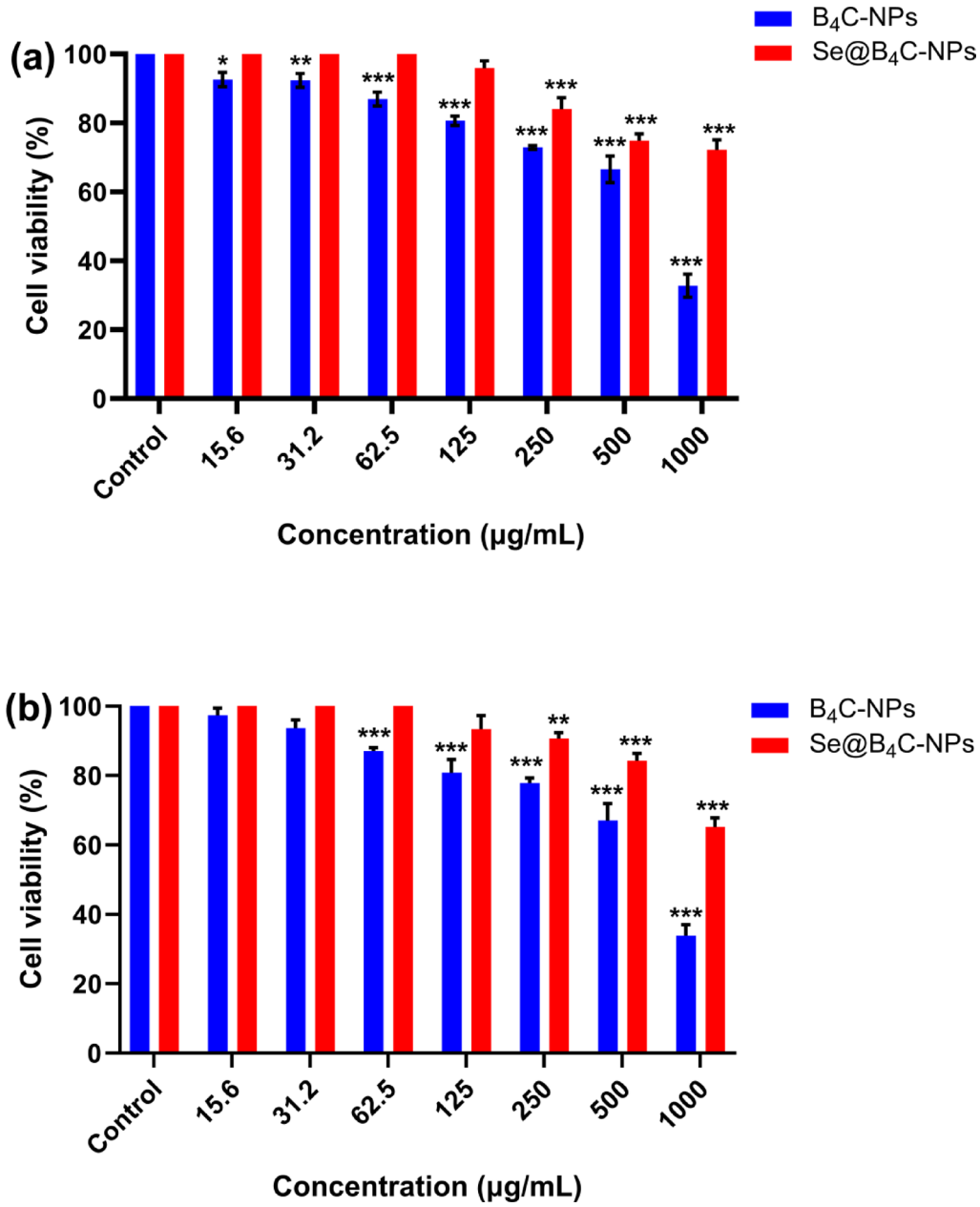

Fig. 14. The viability (%) of HFFs treated with various concentrations (15.6–1000 µg/mL) of B_4C-NPs and Se@B_4C-NPs when compared to the control (untreated) group after (**a**) 48 and (**b**) 72 h of exposure. Columns represent mean ± standard deviation (SD) of three replicates. Two-way ANOVA was used to make comparisons between each group and the control (untreated) group. $^*p < 0.05$, $^{**}p < 0.01$, and $^{***}p < 0.001$ reflect a significant difference as compared to the control (untreated) group.

size values. In this study, TEM analysis showed that the size of Se@B_4C-NPs was 10.40 nm which was in the range of 1–100 nm.

Recently, B_4C-NPs have been used to remove pollutants from aqueous solution. For example, the efficacy of nanostructured B_4C for removal of the organic dyes methylene blue and synazol yellow was shown[31]. Since the recombination rate of photogenerated electrons and holes considerably affects photocatalytic productivity, the formation of heterojunctions between B_4C, metals, non-metals, and composites can improve their photocatalytic properties. Doping semiconductors with transition metals and non-metals is used to capture the electrons produced by light irradiation to reduce the possibility of electron-hole recombination; hence, in this work, we doped B_4C with Se to improve its photocatalytic activity. Table 3 displays similar studies on the photocatalytic activity of different NPs doped with Se against organic pollutants. So far, no study has reported doping B_4C-NPs with metals or non-metals, nevertheless, the following studies reported B_4C doping with composites: it was explored that coupling B_4C and silver ferrite ($AgFe_2O_4$): ($B_4C/AgFe_2O_4$ composite) could be used to remove Cr (VI) ions[68]. This study reported that during the photoreduction process, the poisonous Cr (VI) ions are

transformed into less harmful Cr (III) by the radicals produced, and removed from the aqueous solution. In another study, B_4C/SnO_2 NPs were used to remove dyes such as Novacron red Huntsman (NRH) and methylene blue[69]. Moreover, $BiOI/B_4C$ photocatalyst was used to remove bisphenol S[70].

Sample	Organic pollution	Irradiation time (min)	η (%)	Ref
Se-doped nickel oxide NPs	MB	200	76	63
Se-doped TiO_2/ TiO_2	RhB	300	91.3/ 60.3	71
Se-doped ZnO NPs	TB	360	89.2	72
Se-doped ZnS/ ZnS NPs	TB	180	99/ 38	73
Se-doped SiO_2 nanocomposite	MG	40	97	74
Se@B_4C-NPs/ B_4C-NPs	MB	60	83/ 51	This work

Table 3. The enhanced photocatalytic activity of Se-doped NPs for degradation of organic pollutants.*Se* Selenium, *NPs* Nanoparticles, *MB* Methylene blue, *TB* Trypan blue, *RhB* Rhodamine B, *MG* Methyl green.

In a previous attempt to remove 3-MCPD via photolysis under UV irradiation, it was indicated that in the absence of H_2O_2, essentially no chemical loss was observed within 15 min at pH 5 [11]. Nevertheless, the addition of H_2O_2 resulted in photochemical formation of hydroxyl radicals that react with 3-MCPD. Our study also showed that visible light-only irradiation could not degrade 3-MCPD in the absence of NPs. In photolysis, photons break down compounds and the interaction between these photons and the target molecule leads to the destruction of the molecule. Our study shows that utilization of NPs could result in pronounced photocatalytic activity against 3-MCPD. This difference could be due to variations in experimental conditions, such as light source, 3-MCPD concentrations, and use of NPs. Additionally, doping with Se in our study might have contributed to enhanced photocatalytic activity. To understand the photocatalytic reaction mechanism of Se@B_4C-NPs which has a heterostructure, it is essential to find the position of the valence band (VB) and conduction band (CB). The actual band position can be estimated by identifying the flat-band potential calculated using the electronegativity of the semiconductor[75]. The potentials of the conduction band (CB) and valence band (VB) at the point of zero charge is calculated using the following Eq.[76]:

$$E_{VB} = X - E_0 + 0.5Eg \tag{4}$$

$$E_{CB} = E_{VB} - Eg \tag{5}$$

Where X is the electronegativity of semiconductors according to Pearson (1987)[77]. Additionally, Eg refers to the band gap energy, and E_0 indicates the energy of free electrons relative to the standard hydrogen electrode (4.5 eV). For B_4C-NPs, the X was 4.628 eV and the E_{CB} and E_{CV} were −0.657 eV and 0.913 eV, respectively. The X for Se@B_4C-NPs was 4.818 eV and the E_{CB} and E_{CV} were −0.412 eV and 1.048 eV, respectively. The corresponding band gap energies for B_4C-NPs and Se@B_4C-NPs were 1.57 eV and 1.46 eV, respectively. Further details on the band gap calculation for B_4C-NPs and Se@B_4C-NPs are given in Sect. 3.7. The interaction of Se doping with B_4C-NPs influences the charge transfer pathway, suppressing recombination for photogenerated charges. Mechanistically, electrons move towards the CB to produce photocatalytic activity, but it is possible for B_4C-NPs that some excited electrons return to the VB without participating in the photocatalytic process, i.e. the electron-hole recombination occurs and induces low photocatalytic efficiency. In a study using Se-doped g-C_3N_4 nanosheets, it was reported that some excited electrons were stuck in Deep Traps (DTs), making them inactive and do not allow them to participate in the photocatalytic activity. In comparison, following Se doping, some Shallow Traps (STs) are created near the CB, and this phenomenon contributes to improved photocatalytic performance. After excitation, the STs capture electrons that are moving towards the VB, thus hindering the recombination of charge carriers[36].

Moreover, the present study of the role of scavengers in the photocatalytic function showed the generation of both hydroxyl and superoxide anion radicals. These superoxide anion radicals can indirectly produce hydroxyl radicals which are the main factor in the degradation of 3-MCPD and help to further degrade the chemical.

Figure 15 depicts a schematic presentation of possible mechanisms underlying the photocatalytic function of Se@B_4C-NPs. When B_4C-NPs are exposed to visible light and the photon energy (hυ) is ≥Eg, electrons occupying the VB are induced to an empty CB. This leads to the formation of electron-hole (e^-/h^+) pairs (Eq. 6). The e^-/h^+ pairs are transferred to the surface of B_4C-NPs and initiate a redox reaction. Then, hydroxyl radicals are formed via a reaction of h^+ with water and hydroxide ions (Eqs. 7 and 8), and finally, superoxide anion radical is generated via a reaction of e^- with oxygen (Eq. 9). Hydroxyl and superoxide radicals attack 3-MCPD on B_4C-NPs surface and form intermediate degradation products (Eq. 12). The C-Cl bond in 3-MCPD is relatively weak, making it susceptible to hemolytic cleavage after radical formation. In this step, 3-MCPD radical might release a chlorine radical (Cl°) and form a reactive alkene or alcohol intermediate (Eq. 13). The allylic radical can react with molecular oxygen (O_2) to form Peroxyl radicals (ROO°) which may lead to further degradation and breakdown of 3-MCPD into smaller organic acids, aldehydes, or CO_2 (Eqs. 14 and 15)[78].

$$h\nu\ (Visible) + Se@\ B_4C - NPs \rightarrow Se@B_4C - NPs\left(\ h^+_{VB} + e^-_{CB}\ \right) \tag{6}$$

$$Se@\ B_4C - NPs\left(h^+_{VB}\right) + H_2O \rightarrow\ Se@\ B_4C - NPs + H^+ + OH^- \tag{7}$$

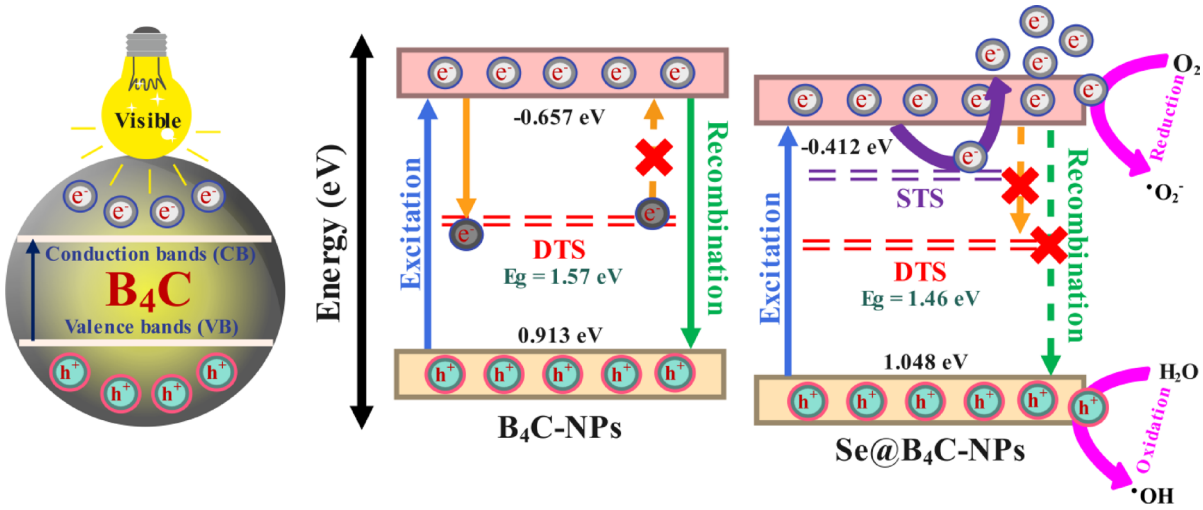

Fig. 15. A schematic depiction and proposed mechanism of photocatalytic activity of Se@B_4C-NPs. *DTs* Deep Traps, *STs* Shallow Traps, *NPs* Nanoparticles, *B_4C-NPs* boron carbide nanoparticles, and *Se@ B_4C-NPs* Se-doped B_4C-NPs.

$$Se@\,B_4C-NPs\left(h^{+}_{VB}\right)+OH^{-}\rightarrow\ Se@\,B_4C-NPs+OH^{\circ} \tag{8}$$

$$Se@\,B_4C-NPs\left(e^{-}_{CB}\right)+O_2\rightarrow\ Se@\,B_4C-NPs+^{\circ}\ O_2^{-} \tag{9}$$

$$^{\circ}\,O_2^{-}+2H^{+}\rightarrow\ \ H_2O_2 \tag{10}$$

$$H_2O_2+\ h\nu\ \ (Visible)\rightarrow 2\ OH^{\circ} \tag{11}$$

$$3-MCPD+OH^{\circ}or\ ^{\circ}O_2^{-}\ \rightarrow 3-MCPD\ radical+H_2O \tag{12}$$

$$3-MCPD\ radical\ \rightarrow Allylic\ radical+Cl^{\circ} \tag{13}$$

$$Allylic\ radical+\ O_2\ \rightarrow Peroxyl\ radical\ \left(ROO^{\circ}\right) \tag{14}$$

$$Peroxyl\ radical\ \left(ROO^{\circ}\right)\rightarrow CO_2+H_2O+\ \min eral\ acids \tag{15}$$

In our study, Se@B_4C-NPs showed greater photocatalytic activity against 3-MCPD than B_4C-NPs. The degradation yield was investigated by UV-Vis spectrophotometry and LC-MS/MS analysis, which confirmed decreased concentrations of 3-MCPD in water. Our in vitro assessments demonstrated that HFF cells viability upon 48 and 72-h exposure to Se@B_4C-NPs at 125 µg/mL, was >80%. While treatment with B_4C-NPs had an IC50 of 741.1 µg/mL in HFF cells. In a previous study, Singh et al. revealed B_4C-NPs biocompatibility at levels up to ~800 µg/mL in HEK-293 cells[31]. In another study, an IC_{20} 202.525 mg/L was reported for B_4C-NPs against HPAEpiC cells[79]. As shown in Fig. 14, at concentrations greater than 250 µg/mL, Se@B_4C-NPs showed toxic effect towards HFFs cells. Thus, application of these materials should be considered with caution at these concentrations, however, due to lack of information on large scale usage of NPs imposing cytotoxicity, more assessments need to be performed in this regard.

Conclusion

In conclusion, this study successfully synthesized and characterized Se@B_4C-NPs, we have demonstrated the potential of these NPs for effective photocatalytic removal of 3-MCPD from aqueous solution. In this work, we synthesized Se@B_4C-NPs at low temperatures and in a short time compared to B_4C-NPs. FT-IR, FE-SEM/EDX XRD, DLS, PZ, and UV–Vis/DRS data was used to characterize the synthesized particles. The structural characterization confirmed the successful integration of Se into B_4C-NPs which occurred with significant impacts on the XRD pattern, PL, and morphology determination. TEM analyses revealed the spiral structure of B_4C-NPs which remained unchanged after doping. The photocatalytic studies highlighted the synergistic effect of Se@B_4C-NPs and visible radiation in reducing the concentration of 3-MCPD. The photodegradation rate of 3-MCPD for B_4C-NPs and Se@B_4C-NPs was 51% and 83% respectively as determined using UV-Vis spectrophotometry. Also, the analyte's level was determined using LC-MS/MS, and results showed that treatment with B_4C-NPs and Se@B_4C-NPs under light exposure caused respectively, 56% and 88% reduction in 3-MCPD concentration. Moreover, treatment of human foreskin fibroblasts (HFFs) for 48 and 72 h with Se@B_4C-NPs at levels ≥ 250 µg/mL markedly diminished cell viability.

Data availability

Data will be made available upon request sent to Ramin Rezaee (rezaeera@mums.ac.ir or raminrezaee1983@gmail.com).

Received: 21 December 2024; Accepted: 24 June 2025
Published online: 02 July 2025

References

1. Sun, C. et al. Occurrence, formation mechanism, detection methods, and removal approaches for chloropropanols and their esters in food: an updated systematic review. *Food Chemistry: X*. **17**, 100529 (2023).
2. Ioime, P., Piva, E., Pozzebon, M. & Pascali, J. P. Automated sample Preparation and analysis by gas chromatography tandem mass spectrometry (GC–MS/MS) for the determination of 3-and 2-monochloropropanediol (MCPD) esters and glycidol esters in edible oils. *J. Chromatogr. A*. **1650**, 462253 (2021).
3. Eisenreich, A. et al. 3-MCPD as contaminant in processed foods: state of knowledge and remaining challenges. *Food Chem.* **403**, 134332 (2023).
4. Taghizadeh, S. F. et al. Analysis of 3-MCPD and 1, 3-DCP occurrence in mayonnaise: A probabilistic risk assessment of dietary exposure for Iranians. *Toxicol. Rep.* **13**, 101725 (2024).
5. Taghizadeh, S. F. et al. Determination of 3 monochloropropane-1, 2-diol (3-MCPD) level in chocolate: A probabilistic health risk assessment for Iranian consumers. *J. Food Compos. Anal.* **125**, 105800 (2024).
6. Taghizadeh, S. F. et al. Assessment of health risk associated with the occurrence of 3-MCPD in infant formula and baby foods. *J. Food Compos. Anal.* **140**, 107207 (2025).
7. Ahmadpourmir, H. et al. 3-Monochloropropane-1, 2-diol (3-MCPD)(free and esterified) in edible oil, soy sauce and infant formula: A systematic review of the occurrence and employed analytical approaches. *Microchem. J.* 110501 (2024).
8. Taghizadeh, S. F., Rezaee, R., Azizi, M., Hayes, A. W. & Karimi, G. Occurrence of 3-monochloropropane-1, 2-Diol (3-MCPD) in canned vegetables: A probabilistic assessment of health risk for Iranian consumers. *J. Food Compos. Anal.* **115**, 104993 (2023).
9. Walker, R. Risk assessment of ochratoxin: current views of the European scientific committee on food, the JECFA and the Codex committee on food additives and contaminants. *Mycotoxins Food Saf.* 249–255 (2002).
10. Humans, I. W. G. O. T. E. o. C. R. T. Some chemicals present in industrial and consumer products, food and drinking-water. *IARC Monogr. Eval. Carcinog. Risks Hum.* **101**, 9 (2013).
11. Nienow, A. M., Poyer, I. C., Hua, I. & Jafvert, C. T. Hydrolysis and H2O2-assisted UV photolysis of 3-chloro-1, 2-propanediol. *Chemosphere* **75**, 1015–1020 (2009).
12. Tollini, F. et al. Influence of pH on the kinetics of hydrolysis reactions: the case of epichlorohydrin and glycidol. *Reaction Chem. Eng.* **7**, 2211–2223 (2022).
13. Fattore, E. et al. Toxicology of 3-monochloropropane-1, 2-diol and its esters: a narrative review. *Arch. Toxicol.* **97**, 1247–1265 (2023).
14. Wang, K. L. et al. Alleviating 3-MCPD-induced male reproductive toxicity: mechanistic insights and Resveratrol intervention. *Ecotoxicol. Environ. Saf.* **271**, 115978 (2024).
15. Khan, Z. U. H. et al. Removal of organic pollutants through hydroxyl radical-based advanced oxidation processes. *Ecotoxicol. Environ. Saf.* **267**, 115564 (2023).
16. Ishwarya, S., Nagaswarupa, H., Naik, R. & Basavaraju, N. Multifunctional applications of novel copper magnesium vanadate nanoparticles: photocatalytic dye degradation and electrochemical properties. *Microchem. J.* **206**, 111489 (2024).
17. Nidheesh, P. V. et al. Electro-Fenton process in combination with other advanced oxidation processes: challenges and opportunities. *Curr. Opin. Electrochem.* **37**, 101171 (2023).
18. Al-Nuaim, M. A., Alwasiti, A. A. & Shnain, Z. Y. The photocatalytic process in the treatment of polluted water. *Chem. Pap.* **77**, 677–701 (2023).
19. Zhou, L. et al. Insight on photocatalytic synchronous oxidation and reduction for pollutant removal: chemical energy conversion between macromolecular organic pollutants and heavy metal. *J. Hazard. Mater.* **477**, 135236 (2024).
20. Younas, M. U. et al. Biogenic synthesis of zinc oxide nanoparticles using NARC G1 Garlic (Allium sativum) extract, their photocatalytic activity for dye degradation and antioxidant activity of the extract. *Results Chem.* **13**, 102035 (2025).
21. Velayati, M. et al. Xanthan gum-mediated green synthesis of Se-nanoparticles for evaluation of photocatalytic and cytotoxicity effects. *Eur. Phys. J. Plus*. **138**, 947 (2023).
22. Safa, S., Hejazi, R., Rabbani, M. & Azimirad, R. Hydrothermal synthesis of NiO nanostructures for photodegradation of 4-nitrophenol. *Desalination Water Treat.* **57**, 21982–21989 (2016).
23. Qiao, H., Wei, Z., Yang, H., Zhu, L. & Yan, X. Preparation and characterization of NiO nanoparticles by anodic arc plasma method. *J. Nanomater.* **2009** 795928. (2009).
24. Du, Y. et al. Preparation of NiO nanoparticles in microemulsion and its gas sensing performance. *Mater. Lett.* **68**, 168–170 (2012).
25. Alagiri, M., Ponnusamy, S. & Muthamizhchelvan, C. Synthesis and characterization of NiO nanoparticles by sol–gel method. *J. Mater. Sci.: Mater. Electron.* **23**, 728–732 (2012).
26. Eizi, R., Bastami, T. R., Mahmoudi, V., Ayati, A. & Babaei, H. Facile ultrasound-assisted synthesis of CuFe-Layered double hydroxides/g-C_3N_4 nanocomposite for Alizarin red S sono-sorption. *J. Taiwan Inst. Chem. Eng.* **145**, 104844 (2023).
27. Rahmat, M. et al. Laser ablation assisted Preparation of MnO_2 nanocolloids from waste battery cell powder: evaluation of physico-chemical, electrical and biological properties. *J. Mol. Struct.* **1191**, 284–290 (2019).
28. Anandan & Rajendran, V. Morphological and size effects of NiO nanoparticles via solvothermal process and their optical properties. *Mater. Sci. Semiconduct. Process.* **14**, 43–47 (2011).
29. Younas, M. U., Usman, A., Kashif, A. R., Zahoor, A. & Haider, F. Green synthesis of TiO_2 NPs using agave americana leaves: Antioxidant, cytotoxicity, and photocatalytic activity. *ChemistrySelect* **9** e202404050 (2024).
30. Zhou, H. et al. Degradation of TCH by Fe_3O_4/B_4C catalyzed heterogeneous Fenton oxidation. *J. Alloys Compd.* **995**, 174787 (2024).
31. Singh, P. et al. Nanostructured Boron carbide (B_4C): A bio-compatible and recyclable photo-catalyst for efficient wastewater treatment. *Materialia* **1**, 258–264 (2018).
32. Hamd, S. S., Ramizy, A. & Ismail, R. A. Preparation of novel B_4C nanostructure/si photodetectors by laser ablation in liquid. *Sci. Rep.* **12**, 16529 (2022).
33. Hasanah, A. U., Gareso, P. L., Rauf, N. & Tahir, D. Photocatalytic performance of zinc oxide and Metal-Doped zinc oxide for various organic pollutants. *ChemBioEng Reviews*. **10**, 698–710 (2023).
34. Li, R. et al. Novel visible-light activated photocatalytic ultrafiltration membrane for simultaneous separation and degradation of emerging contaminants. *J. Hazard. Mater.* **478**, 135634 (2024).
35. Starukh, H. & Praus, P. Doping of graphitic carbon nitride with non-metal elements and its applications in photocatalysis. *Catalysts* **10**, 1119 (2020).
36. Rehman, Z. U. et al. Selenium doping to improve internal electric field for excellent photocatalytic efficiency of g-C_3N_4 nanosheets. *Sep. Purif. Technol.* **350**, 128001 (2024).

37. Strijowski, U., Heinz, V. & Franke, K. Removal of 3-MCPD esters and related substances after refining by adsorbent material. *Eur. J. Lipid Sci. Technol.* **113**, 387–392 (2011).
38. Şahin, T., Ok, S. & Yılmaz, E. Application of MOFs and natural clays for removal of MCPD and GEs from edible oils. *Grasas Y Aceites*. **73**, e461–e461 (2022).
39. Yanase, I., Ogawara, R. & Kobayashi, H. Synthesis of Boron carbide powder from Polyvinyl Borate precursor. *Mater. Lett.* **63**, 91–93 (2009).
40. Koysuren, O. & Koysuren, H. N. Preparation and activity evaluation of B4C/ZnO composite photocatalyst. *J. Solgel Sci. Technol.* **103**, 172–184 (2022).
41. Velayati, M., Hassani, H., Sabouri, Z., Mostafapour, A. & Darroudi, M. Biosynthesis of Se-Nanorods using gum Arabic (GA) and investigation of their photocatalytic and cytotoxicity effects. *Inorg. Chem. Commun.* **128**, 108589 (2021).
42. Li, J. et al. Fabrication of multi-morphological Bi_2O_2 (OH) NO_3-$BiVO_4$ Z-Scheme heterojunction for enhanced photocatalytic antibiotic removal performance. *J. Environ. Chem. Eng.* **11**, 110962 (2023).
43. Khalef, L., Lydia, R., Filicia, K. & Moussa, B. Cell viability and cytotoxicity assays: biochemical elements and cellular compartments. *Cell Biochem. Funct.* **42**, e4007 (2024).
44. Yıldırım, A., Aksoy, T. & Balcıoğlu, İ. C. Comparative assessment of colorimetric assays in evaluating intracellular drug susceptibility of leishmania tropica against conventional antileishmanial drugs. *Parasitol. Int.* **106**, 103021 (2025).
45. Fathi, A., Ehsani, N., Rashidzadeh, M., Baharvandi, H. & Rahimnejad, A. Synthesis of Boron carbide nano particles using Polyvinyl alcohol and boric acid. *Ceram.-Silik.* **56**, 32–35 (2012).
46. Aydın, H. & Tuncer, E. Synthesis and characterization of mechanical activation assisted Boron carbide (B_4C) precursor powders. *J. Sci. Rep. A* 79–97 (2022).
47. Velayati, M., Hassani, H. & Darroudi, M. Green synthesis of Se-Nanorods using Poly anionic cellulose (PAC) and examination of their photocatalytic and cytotoxicity effects. *Inorg. Chem. Commun.* **133**, 108935 (2021).
48. El-Sayed, S. A. & Mostafa, M. Pyrolysis characteristics and kinetic parameters determination of biomass fuel powders by differential thermal gravimetric analysis (TGA/DTG). *Energy. Conv. Manag.* **85**, 165–172 (2014).
49. Kakiage, M., Tahara, N., Yanagidani, S., Yanase, I. & Kobayashi, H. Effect of Boron oxide/carbon arrangement of precursor derived from condensed polymer-boric acid product on low-temperature synthesis of Boron carbide powder. *J. Ceram. Soc. Jpn.* **119**, 422–425 (2011).
50. Gu, Y., Chen, L., Qian, Y., Zhang, W. & Ma, J. Synthesis of nanocrystalline Boron carbide via a solvothermal reduction of CCl4 in the presence of amorphous Boron powder. *J. Am. Ceram. Soc.* **88**, 225–227 (2005).
51. Feiz, S. F., Nikzad, L., Majidian, H. & Salahi, E. Synthesizability improvement of B_4C ceramics by optimizing the process temperature and atmosphere. *Synthesis Sinter.* **2**, 181–185 (2022).
52. Velayati, M. et al. Thermal stability investigation of synthesized epoxy-polyurethane/silica nanocomposites. *Silicon* 1–14 (2022).
53. Avcioglu, S., Kaya, F. & Kaya, C. Non-catalytic synthesis of Boron carbide (B_4C) nano structures with various morphologies by sol-gel process. *Mater. Lett.* **249**, 201–205 (2019).
54. ShekoftehNarm, T., Hamidinezhad, H., Sabouri, Z. & Darroudi, M. Plant-based synthesis of Selenium-doped silver/magnesium oxide/zinc oxide nanocomposite using Mentha Pulegium to investigate their photocatalytic and biological properties. *J. Mol. Struct.* 139678 (2024).
55. Vinokurov, A., Chernysheva, G., Mordvinova, N. & Dorofeev, S. Optical properties and structure of Ag-doped inp quantum Dots prepared by a phosphine synthetic route. *Dalton Trans.* **47**, 12414–12419 (2018).
56. García-Valdivieso, G. et al. Ag@ zno/mwcnt ternary nanocomposite as an active and stable catalyst for the 4-nitrophenol reduction in water. *Nanotechnology* **32**, 315713 (2021).
57. Groeneveld, I., Kanelli, M., Ariese, F. & van Bommel, M. R. Parameters that affect the photodegradation of dyes and pigments in solution and on substrate–An overview. *Dyes Pigm.* **210**, 110999 (2023).
58. Aisien, F., Amenaghawon, N. & Ekpenisi, E. Photocatalytic decolourisation of industrial wastewater from a soft drink Compan. *UNIZIK J. Eng. Appl. Sci.* **9**, 11–16 (2013).
59. Fan, G. et al. Rapid synthesis of ag/agcl@ ZIF-8 as a highly efficient photocatalyst for degradation of acetaminophen under visible light. *Chem. Eng. J.* **351**, 782–790 (2018).
60. Brindhadevi, K. et al. Enhanced photocatalytic degradation of polycyclic aromatic hydrocarbons (PAHs) using NiO nanoparticles. *Environ. Res.* **252**, 118454 (2024).
61. Saadabadi, R. H., Tehrani, F. S., Darroudi, M. & Sabouri, Z. Plant-based synthesis of ZnO–CeO_2–MgO nanocomposite using Ocimum Basilicum L seed extract: biological effects and photocatalytic activity. *Mater. Chem. Phys.* **314**, 128919 (2024).
62. Sharma, V. et al. The effect of calcination temperatures on the structural and optical properties of zinc oxide nanoparticles and their influence on the photocatalytic degradation of leather dye. *Chem. Phys. Impact*. **6**, 100196 (2023).
63. Ghazal, S. et al. Sol-gel synthesis of selenium-doped nickel oxide nanoparticles and evaluation of their cytotoxic and photocatalytic properties. *Inorg. Chem. Res.* **5**, 37–49 (2021).
64. Anguraj, G. et al. MnO_2 doped with ag nanoparticles and their applications in antimicrobial and photocatalytic reactions. *Catalysts* **13**, 397 (2023).
65. Mourdikoudis, S., Pallares, R. M. & Thanh, N. T. Characterization techniques for nanoparticles: comparison and complementarity upon studying nanoparticle properties. *Nanoscale* **10**, 12871–12934 (2018).
66. Urquidi, O., Brazard, J. & Adachi, T. B. *Applied Optical Metrology V*. 85–91 (SPIE).
67. Khan, H. et al. Experimental methods in chemical engineering: X-ray diffraction spectroscopy—XRD. *Can. J. Chem. Eng.* **98**, 1255–1266 (2020).
68. Koysuren, O. & Koysuren, H. N. Photoreduction of cr (VI) on B4C/AgFe2O4 composite. *J. Solgel Sci. Technol.* **105**, 220–236 (2023).
69. Singh, P. et al. Specially designed B_4C/SnO_2 nanocomposite for photocatalysis: traditional ceramic with unique properties. *Appl. Nanosci.* **8**, 1–9 (2018).
70. Lv, Y. et al. Bisphenol S degradation by visible light assisted peroxymonosulfate process based on BiOI/B_4C photocatalysts with Z-scheme heterojunction. *Chem. Eng. J.* **417**, 129188 (2021).
71. Xie, W., Li, R. & Xu, Q. Enhanced photocatalytic activity of Se-doped TiO_2 under visible light irradiation. *Sci. Rep.* **8**, 8752 (2018).
72. Nenavathu, B. P., Rao, A. K., Goyal, A., Kapoor, A. & Dutta, R. K. Synthesis, characterization and enhanced photocatalytic degradation efficiency of se doped ZnO nanoparticles using Trypan blue as a model dye. *Appl. Catal. A*. **459**, 106–113 (2013).
73. Talukdar, S. & Dutta, R. K. A mechanistic approach for superoxide radicals and singlet oxygen mediated enhanced photocatalytic dye degradation by selenium doped ZnS nanoparticles. *RSC Adv.* **6**, 928–936 (2016).
74. Ganapathi, A. Se-doped SiO_2 nancomposite material synthesis, characterization and multi applications. *Mater. Sci. Energy Technol.* **5**, 161–170 (2022).
75. ShekoftehNarm, T., Hamidinezhad, H., Sabouri, Z. & Darroudi, M. Plant-based synthesis of Selenium-doped silver/magnesium oxide/zinc oxide nanocomposite using Mentha pulegium to investigate their photocatalytic and biological properties. *J. Mol. Struct.* **1320**, 139678 (2025).
76. Jeyakanthan, M., Subramanian, U. & Tangsali, R. Enhanced photoluminescence of $CoWO_4$ in $CoWO_4$/$PbWO_4$ nanocomposites. *J. Mater. Sci.: Mater. Electron.* **29**, 1914–1924 (2018).
77. Pearson, R. G. Absolute electronegativity and hardness: application to inorganic chemistry. *Inorg. Chem.* **27**, 734–740 (1988).
78. Nenavathu, B., Sharma, A. & Dutta, R. K. Se doped ZnO nanoparticles with improved catalytic activity in degradation of cholesterol. *J. Water Environ. Nanatechnol.* **3**, 289–300 (2018).

79. Türkez, H. et al. Microarray assisted toxicological investigations of Boron carbide nanoparticles on human primary alveolar epithelial cells. *Chemico-Biol. Interact.* **300**, 131–137 (2019).

Acknowledgements
The authors are thankful to Vice Chancellor of Research, Mashhad University of Medical Sciences, Mashhad, Iran, for the financial support (Project No. 4021484 and Ethics committee approval No. IR.MUMS.MEDICAL.REC.1402.396).

Author contributions
M.V., R.R., and T.R.B. conceptualized and designed the study. M.V., R.R., T.R.B. and H.Ahmadzadeh designed the experiments and M.V. gathered data. S. N. conducted the in vitro analysis. M.V., S. F. T., H. R., and R. R. wrote the main manuscript text. M.V., S.N., and H.A. prepared Figures. R.R., T.R.B, R. K. O. and H.Ahmadzadeh critically revised the manuscript. All authors reviewed the manuscript and approved the final version for submission.

Declarations

Competing interests
The authors declare no competing interests.

Additional information
Correspondence and requests for materials should be addressed to H.A. or R.R.

Reprints and permissions information is available at www.nature.com/reprints.

Publisher's note Springer Nature remains neutral with regard to jurisdictional claims in published maps and institutional affiliations.